OPEN ACCESS

University of Dundee

University of Dundee

Tissue environment, not ontogeny, defines murine intestinal intraepithelial T lymphocytes

Brenes, Alejandro; Vandereyken, Maud; James, Olivia J.; Watt, Harriet; Hukelmann, Jens; Spinelli, Laura

Published in:
eLife

DOI:
10.7554/eLife.70055

Publication date:
2021

Document Version
Peer reviewed version

Link to publication in Discovery Research Portal

Citation for published version (APA):
Brenes, A., Vandereyken, M., James, O. J., Watt, H., Hukelmann, J., Spinelli, L., Dikovskaya, D., Lamond, A. I., & Swamy, M. (2021). Tissue environment, not ontogeny, defines murine intestinal intraepithelial T lymphocytes. *eLife*, *10*, [e70055]. https://doi.org/10.7554/eLife.70055

General rights
Copyright and moral rights for the publications made accessible in Discovery Research Portal are retained by the authors and/or other copyright owners and it is a condition of accessing publications that users recognise and abide by the legal requirements associated with these rights.

- Users may download and print one copy of any publication from Discovery Research Portal for the purpose of private study or research.
- You may not further distribute the material or use it for any profit-making activity or commercial gain.
- You may freely distribute the URL identifying the publication in the public portal.

Take down policy
If you believe that this document breaches copyright please contact us providing details, and we will remove access to the work immediately and investigate your claim.

Download date: 27. Sep. 2021

Tissue environment, not ontogeny, defines murine intestinal intraepithelial T lymphocytes

Alejandro J. Brenes[1,3#], Maud Vandereyken[2#], Olivia J. James[2], Harriet Watt[2], Jens Hukelmann[1§], Laura Spinelli[3], Dina Dikovskaya[2], Angus I. Lamond[1], Mahima Swamy[2,3*]

[1]Centre for Gene Regulation and Expression, [2]MRC Protein Phosphorylation and Ubiquitylation Unit, [3]Division of Cell Signalling and Immunology, School of Life Sciences, University of Dundee, Dundee DD1 5EH, United Kingdom

[§]Present Address: Immatics, Paul-Ehrlich-Str. 15, Tuebingen, 72076, Germany

*Address correspondence to: Dr. Mahima Swamy, Email: m.swamy@dundee.ac.uk

[#]These authors contributed equally

Abstract

Tissue-resident intestinal intraepithelial T lymphocytes (T-IEL) patrol the gut and have important roles in regulating intestinal homeostasis. T-IEL include both induced T-IEL, derived from systemic antigen-experienced lymphocytes, and natural IEL, which are developmentally targeted to the intestine. While the processes driving T-IEL development have been elucidated, the precise roles of the different subsets and the processes driving activation and regulation of these cells remain unclear. To gain functional insights into these enigmatic cells, we used high-resolution, quantitative mass spectrometry to compare the proteomes of induced T-IEL and natural T-IEL subsets, with naive $CD8^+$ T cells from lymph nodes. This data exposes the dominant effect of the gut environment over ontogeny on T-IEL phenotypes. Analyses of protein copy numbers of >7000 proteins in T-IEL reveal skewing of the cell surface repertoire towards epithelial interactions and checkpoint receptors; strong suppression of the metabolic machinery indicating a high energy barrier to functional activation; upregulated cholesterol and lipid metabolic pathways, leading to high cholesterol levels in T-IEL; suppression of T cell antigen receptor signalling and expression of the transcription factor TOX, reminiscent of chronically activated T cells. These novel findings illustrate how T-IEL integrate multiple tissue-specific signals to maintain their homeostasis and potentially function.

Introduction

The presence of tissue resident immune cells enables a quick response to either local stress, injury or infection. Understanding the functional identity of immune cells and their shaping by the tissue environment is therefore critical to understanding tissue immunity. Intestinal intraepithelial T lymphocytes (T-IEL) reside within the intestinal epithelium and consist of a heterogenous mix of natural and induced T-IEL (Olivares-Villagómez and Van Kaer, 2018). All T-IEL express a T cell antigen receptor (TCR), consisting of either αβ, or γδ chains, alongside TCR co-receptors, i.e., CD8αβ or CD8αα and to a lesser extent CD4(+/-). The most prevalent IEL subsets within the epithelium of the murine small intestine are derived directly from thymus progenitors, so-called natural, or unconventional T-IEL. These natural T-IEL express either TCRγδ and CD8αα (TCRγδ CD8αα T-IEL), which account for ~50% of the total T-IEL pool, or express TCRαβ and CD8αα (TCRβ CD8αα T-IEL), which account for ~25% of the total T-IEL. TCRβ CD8αα T-IEL are derived from $CD4^-CD8^-$ double negative (DN) progenitors in the thymus by agonist selection. Conversely, induced T-IEL are antigen-experienced, conventional $CD4^+$ or $CD8\alpha\beta^+$ αβ T cells that are induced to establish tissue-residency within the intestinal epithelium, most likely in response to cues from dietary antigens and the microbiota, as evidenced by a strong reduction in their numbers in germ-free and protein antigen-free mice (Di Marco Barros et al., 2016). These induced T-IEL (TCRβ CD8αβ T-IEL) are believed to have substantial overlap with tissue-resident memory T (T_{RM}) cells (Sasson et al., 2020) and are present in high numbers in human intestines. How these induced T-IEL are formed, their functional importance, and the role of the gut environment in deciding their fate are still the focus of intense study.

Residing at the forefront of the intestinal lumen, T-IEL are exposed to a range of commensal bacteria and their metabolites, dietary metabolites and antigens, and potential pathogens. These immune cells are therefore faced with the conflicting tasks of protecting the intestinal barrier, while also preventing indiscriminate tissue damage. Previous gene expression studies have identified T-IEL as having an 'activated-yet-resting' phenotype, with the expression of several activation markers, such as Granzymes and CD44, along with inhibitory receptors, such as the Ly49 family and CD8αα (Denning et al., 2007; Fahrer et al., 2001; Shires et al., 2001). Yet it is still unclear how T-IEL are kept in check at steady-state (Vandereyken et al., 2020). T-IEL effector responses can get dysregulated in chronic inflammatory conditions, such as celiac disease and inflammatory bowel diseases, therefore we need insight into the regulation of these cells. Moreover, we lack an understanding of how T-IEL are programmed to respond to specific epithelial signals, and how this is dictated and regulated by the tissue microenvironment.

In this study, we use quantitative proteomics to explore the differences between induced T-IEL and systemic T cells from lymph nodes (LN), from which induced T-IEL are ostensibly derived. We also compare induced T-IEL with the natural TCRγδ and TCRαβ T-IEL subsets in the gut. Our findings suggest that the tissue environment largely overrides any developmental imprinting of the cells to define the proteomic landscape of intestinal resident T-IEL, and reveal important metabolic and protein translation constraints to T-IEL activation. Importantly, we also uncover evidence of chronic T cell activation potentially driving a partially exhausted phenotype in both the induced and natural T-IEL subsets.

Results

Tissue microenvironment defines intestinal T-IEL as distinct from systemic T cells

$CD8^+$ T-IEL subsets were purified from wild type (WT) murine small intestinal epithelial preparations to greater than 95% purity by cell sorting (***Figure 1— figure supplement 1***). Next, high resolution mass spectrometry (MS) was performed to obtain an in-depth characterisation of the proteomes of the three main $CD8^+$ T-IEL subsets in the intestine. Tandem mass tags (TMT) were used with synchronous precursor selection (SPS) to obtain the most accurate quantifications for all populations (***Figure 1a***). To evaluate how T-IEL related to other immune populations, we first compared the proteomes of T-IEL with other TMT-based proteomes of various T cell populations currently available within the Immunological Proteome Resource (ImmPRes http://immpres.co.uk), an immune cell proteome database developed in-house (Howden et al., 2019). Even though T-IEL are thought to have an effector-like phenotype, by using Principal Component Analysis (PCA), we found that T-IEL were much more similar to *ex-vivo* naïve $CD8^+$ T cells, than to *in-vitro* activated, effector cytotoxic T cells (CTL) (***Figure 1b***). Hence, we did an in-depth, protein-level comparison of the three T-IEL subsets with two naïve $CD8^+$ T cells from the lymph nodes (LN). The two LN naïve $CD8^+$ T cells used here, were either derived from WT mice, similar to the T-IEL, or from P14 transgenic mice, which express a T cell antigen receptor (TCR) specific for a peptide derived from lymphocytic choriomeningitis virus (LCMV). P14 T cells were included as a genetically and developmentally distinct comparator for WT LN T cells. To enable cross-comparisons, all 5 populations were acquired using the same TMT-based SPS-MS3 method and they were all analysed together using MaxQuant (Cox and Mann, 2008). The data were searched using a 1% false discovery rate (FDR) at the protein and peptide spectrum match (PSM) level (for more details see methods). This provided an in-depth overview of the proteome, with over 8,200 proteins detected in total, where each of the 5 populations showed similar coverage, ranging from 6,500 to 7,500 proteins detected in all of them (***Figure 1c***).

For all downstream analyses we converted the raw mass spectrometry intensity values into estimated protein copy numbers using the 'proteomic ruler' (Wisniewski et al., 2014). First, these copy numbers were used to estimate the total protein content for all 5 populations, which revealed no major differences in most, except for the TCRγδ CD8αα T-IEL which displayed a slightly higher protein content than the rest (***Figure 1d***). Next, the copy numbers were used as input for a second dimensionality reduction analysis via PCA, focussed now on comparing the T-IEL and LN populations. The results indicated that across the first component, which explains 44% of variance, there was a clear separation between T-IEL and LN populations (***Figure 1e***), highlighting that the 3 T-IEL subsets share much closer identity to each other, than to the naïve LN T cell populations.

To explore these results further we compared each population to each other. As induced TCRαβ CD8αβ T-IEL are thought to be derived from systemic T cells that respond to antigen in organised lymphoid structures, and then migrate into intestinal tissues, we first compared their proteome to the systemic WT LN TCRαβ CD8αβ T cells. Unexpectedly, the Pearson correlation coefficient comparing the estimated protein copy number of TCRαβ CD8αβ T- IEL and the WT LN TCRαβ CD8αβ T cells, was only 0.85, the lowest value in all the comparisons (***Figure 1f***). In contrast, the proteomes of induced T-IEL and the so-called natural T-IEL populations, showed greater similarity with a correlation >0.93 (***Figure 1g,h***), while the correlation between

LN T cells from WT to P14 TCR transgenic mice was 0.92 (***Figure 1i***). These analyses indicated that induced T-IEL share a very similar expression profile to natural T-IEL. The comparisons to LN T cells revealed that even LN T cells derived from two different strains of mice were much more similar to each other than to induced T-IEL.

To further explore similarities and differences between induced T-IEL and LN T cells we focussed on the TCRαβ CD8αβ T-IEL and the WT LN TCRαβ CD8αβ T cells (LN). We first performed a global analysis of the most abundant protein families that represent the top 50% of the proteome. This overview revealed some similarities and some important proteomic differences between the two cell types. Though the histone content and the glycolytic enzymes looked very similar, there were big differences in proteins related to the ribosomes, the cytoskeleton and the cytotoxic granules (***Figure 2a***). The LN population had nearly double the number of ribosomal proteins, while the T-IEL displayed higher cytoskeletal and cytotoxic proteins. These proteomic differences were not exclusive to TCRαβ CD8αβ T-IEL, as the same pattern was observed within both natural T-IEL subsets. Perhaps the most striking difference between naïve LN T cells and T-IEL was the expression levels of Granzymes (***Figure 2b***). Granzyme A (GzmA) was expressed at >20 million copies per cell in each of the natural T-IEL subsets, and at 9-10 million molecules per cell in the induced T-IEL population. This was more than double what was previously identified in cytotoxic $CD8^+$ T cells (Howden et al., 2019). Granzyme B (GzmB), which was expressed at ~20 million copies per cell in CTL, was expressed at between 4 to 10 million copies per cell in all 3 T-IEL subsets. T-IEL also express Granzyme C (GzmC) and K (GzmK), although at <100,000 molecules per cell each (***Figure 2b***), making their general expression of Granzymes either comparable to, or higher than, *in vitro*-generated CTL. This substantial commitment to Granzyme expression is consistent with the expression of the whole cytotoxic machinery, including perforin and key molecules involved in degranulation (***Supplementary File 1*****,** (James et al., 2020)), all of which are either barely detectable, or altogether absent, in the naïve T cells. Thus, these data support the hypothesis that all T-IEL in the gut are geared towards cytotoxic activity.

To obtain an unbiased overview of the differences between the induced T-IEL and the LN T cell populations, we performed an overrepresentation analysis (ORA) focussed on Gene Ontology (GO) terms related to biological processes (***Figure 2c-d; Supplementary Files 2,3***). The data indicated that proteins which were significantly increased in expression in induced T-IEL were highly enriched in cholesterol and lipid metabolism, intestinal absorption and xenobiotic metabolism and processes involving cytoskeletal proteins, such as cell-cell adhesion and integrin-mediated signalling. Conversely, proteins which were significantly higher expressed in LN T cells were enriched for terms relating to ribosomal proteins and ribonuclease P activity.

Downregulation of protein synthesis in T-IEL

Based on the results obtained from the ORA, we next focussed on the protein machinery involved with the ribosomes and protein synthesis. A comparison of the total estimated copy numbers for ribosomal proteins indicated that LN T cells express almost double the amount expressed in any of the T-IEL subsets (***Figure 3a***). This was true for both cytoplasmic and mitochondrial ribosomal proteins, with the latter being the most

reduced in T-IEL, compared to LN T cells. The decreased expression of ribosomal proteins in T-IEL was mirrored by the decreased expression of RNA polymerases I (Pol1) and III (Pol3), which transcribe, respectively, ribosomal RNA and transfer RNA (***Figure 3b***). For the subunits of both the Pol1 and Pol3 complexes, the median fold reduction in T-IEL was greater than 5-fold when compared to LN T cells (***Figure 3- figure supplement 1***). Strikingly, the subunits specific for RNA polymerase II (Pol2), which transcribes protein-coding genes, did not display a reduction in median expression levels. These data suggest that while ribosomal expression is reduced, mRNA pools could potentially still be maintained in T-IEL.

To maintain protein synthesis, consistent uptake of amino acids is generally required. However, our data show that T-IEL express low levels (<2000 copies per cell) of 3 key amino acid transporters, i.e., SLC1A5, SLC7A5 and SLC38A2 (***Figure 3c***), all of which are highly upregulated upon T cell activation with SLC7A5 being expressed at >400,000 copies in effector T cells (Howden et al., 2019). SLC7A5 expression levels have been reported to directly control the expression of ribosomal proteins and other important translation machinery components (Marchingo et al., 2020; Sinclair et al., 2019). The very low levels of amino acid transporters detected in T-IEL is therefore expected to limit protein synthesis. Furthermore, despite having low levels of amino acid transporters, enzymes involved in amino acid catabolism, such as arginase-2 (ARG2) and alanine aminotransferase (Glutamic-Pyruvic Transaminase, GPT), are highly expressed in T-IEL, also suggesting reduced protein synthesis in T-IEL (***Figure 3d***). Interestingly, high expression of ARG2 was also accompanied by upregulated expression of other enzymes from the urea cycle (***Figure 3- figure supplement 1***). Finally, it is also notable that T-IEL express significantly higher levels of PRKR-Like Endoplasmic Reticulum Kinase (PERK), than LN T cells. PERK functions as a global protein synthesis inhibitor, either in the presence of unfolded proteins, or upon low amino acid availability (***Figure 3e***). We therefore decided to measure the protein synthesis rates in T-IEL and LN T cells by O-propargyl puromycin (OPP) incorporation into nascent peptide chains and compared with cycloheximide-treated controls. The data from the OPP assay highlighted almost undetectable levels of protein translation in all 3 T-IEL subsets (***Figure 3f***), which correlated well with the reduced ribosomal content, low expression of amino-acid transporters and high catabolic enzymes identified within the proteomes of T-IEL. In contrast, LN T cells contain more actively translating ribosomes than T-IEL, providing orthogonal validation of the proteomic data. It should be noted that naïve T cells have been reported to have low protein synthesis rates (Wolf et al., 2020), however, our data indicate even lower synthesis rates in T-IEL. Thus, multiple mechanisms appear to be active in T-IEL to keep protein synthesis at a minimum.

T-IEL have a unique metabolic profile

Recent studies have shown a direct correlation between metabolic activity and the rates of protein synthesis in T cells (Argüello et al., 2020). The very low levels of protein synthesis in all 3 T-IEL subsets therefore prompted us to further explore the bioenergetic profile of T-IEL. Globally, we did not find any major differences in the proportion of the T-IEL proteomes dedicated to the major metabolic pathways compared to naïve T cells (***Figure 4a***). We did however find that all 3 T-IEL subsets express substantial levels of the GLUT2 (~5,000 copies) and GLUT3 (~35,000 copies), both facilitative glucose transporters (***Figure 4b***). GLUT2 is normally found in intestinal and other epithelial cells, not in immune cells, and is a low affinity bidirectional glucose transporter. GLUT3 is a high affinity glucose transporter that is thought to be particularly

important in CD8 T cell activation (Geltink et al., 2018). Glucose can be utilised in T cells through either glycolysis, or oxidative phosphorylation (OXPHOS) and the tricarboxylic acid (TCA) cycle that also provides biosynthetic intermediates (Ma et al., 2019). We therefore examined the expression of proteins involved in these pathways in T-IEL. We find that T-IEL express most of the proteins of the glycolytic and TCA pathways at similar levels to naïve T cells (***Figure 4c***). With one exception being the lactate transporters, SLC16A1 and SLC16A3, which even though they are significantly higher than in naïve T cells, are still expressed at very low levels, indicating a low glycolytic potential within these cells. Furthermore, T-IEL have also been shown to have comparably low OXPHOS potential as in naïve T cells (Konjar et al., 2018). Thus, the function of the glucose being taken up through the T-IEL glucose transporters remains unclear.

We also examined the mitochondrial protein content of T-IEL. The total mitochondrial protein content appeared to be significantly reduced, however, all the components of the electron transport chain (ETC) were expressed at similar levels in all T-IEL, as in LN T cells (***Figure 4d***). These data suggest that T-IEL mitochondria have similar respiratory capacity to naïve T cells. Naïve T cells use OXPHOS and fatty acid oxidation (FAO) to maintain their cellular functions. Therefore, we assessed FAO enzyme expression in T-IEL, and found this was also largely similar to naïve T cells (***Figure 4c***). Interestingly, some proteins involved in peroxisomal FAO, including the transporter ABCD4, the key peroxisomal beta-oxidation enzymes acyl-CoA oxidase ACOX1, and Carnitine O-Acetyltransferase (CrAT), were more highly expressed in T-IEL than in naïve T cells. Peroxisomal FAO produces Acetyl CoA, which can be used within the TCA cycle, and NADH, which can be utilised in the ETC, to contribute to energy production. NADH produced during FAO and OXPHOS needs to be transported into the mitochondria through a redox shuttle, and in this context, we find that the glycerol-3-phosphate shuttle is only expressed in T-IEL (***Figure 4e***). Put together, these data suggest that peroxisomes may be a source of fuel to support the low levels of energy produced in T-IEL, and indicate key differences in the metabolic pathways active in T-IEL.

T-IEL have increased lipid biosynthesis and cholesterol metabolism

Our data would seem to indicate that T-IEL have low bioenergetic production and requirements. However, functional annotation of proteins enriched in induced T-IEL indicate over-representation of cholesterol and steroid metabolism pathways, and the metabolism of chemicals and inorganic compounds (***Figure 2c***). T-IEL are highly enriched in proteins involved in xenobiotic metabolism, including members of the UDP glucuronosyl transferase (UGT) family, Glutathione S-transferase (GST) and Cytochrome P450 (CYP) enzymes (***Supplementary File 1***). Detailed examination of the cholesterol biosynthetic pathway indicates almost all the enzymes are expressed highly in all T-IEL, as compared to LN T cells (***Figure 5a***). This pathway is controlled by the master regulator sterol-regulatory element binding protein 2 (SREBP2) (Madison, 2016), which the data show is exclusively expressed within the 3 T-IEL populations (***Figure 5b***). We therefore measured cholesterol content in T-IEL, and found that indeed all 3 subsets have greater than 2.5-fold more cholesterol than naïve LN CD8 T cells (***Figure 5c***).

T-IEL also express the fatty acid transport proteins (FATP2(*Slc27a2*) and FATP4 (*Slc27a4*)), which are necessary for uptake and transport of long chain fatty acids, as well as fatty acid binding proteins (FABP1, 2, 5 and 6), which also contribute to uptake and transport of fatty acids to the endoplasmic reticulum (ER) (***Figure 5d,e***). In addition to the intestinal specific family member, FABP2 (>350,000 copies/cell), the liver

FABP, FABP1 (>200,000 copies/cell), which is highly expressed in the proximal intestine, and the ileal FABP, FABP6 or Gastrotropin (>10,000 copies/cell), are all also highly expressed in all 3 T-IEL subsets (***Figure 5e***). It is interesting to note that FABP5, which was previously identified as being expressed in skin T_{RM} cells, but not in intestinal T_{RM} at the mRNA level (Frizzell et al., 2020), was detected at >200,000 molecules per cell in all 3 T-IEL. Skin T_{RM} appear to use increased exogenous fatty acids uptake to feed into mitochondrial FAO, thus supporting their maintenance and survival (Pan et al., 2017). However, carnitine O-palmitoyl transferase (CPT1A), the rate-limiting enzyme for mitochondrial FAO of long chain fatty acids is expressed at lower levels in T-IEL compared to naive LN T cells (***Figure 4c***). This suggests that the highly increased lipid transporter expression in T-IEL is not solely used to drive FAO.

T-IEL are also enriched in proteins involved in the two major pathways of triacylglycerol (TAG or triglyceride) synthesis expressed in the intestine (***Figure 5f***) (Yen et al., 2015). TAG is hydrophobic and is either stored transiently in the cytosol in lipid droplets or assembled and secreted from enterocytes in apolipoprotein B (ApoB)-containing chylomicrons, or lipoproteins that also contain cholesterol and cholesteryl esters. Surprisingly, T-IEL also express high levels of a key cholesterol esterification enzyme, Acyl CoA:cholesterol acyl transferase 2, ACAT-2 (*Soat2*), which is thought to be specifically expressed in enterocytes (Pan and Hussain, 2012). Esterification of cholesterol increases its hydrophobicity for efficient packaging into lipoproteins. We therefore also explored the expression of enzymes involved in lipoprotein assembly. Lipoprotein assembly involves the packaging of TAG and cholesteryl esters by the microsomal triglyceride transfer protein (MTP, *Mttp*) into ApoB-lipid conjugates, followed by export out of the cells by the core protein complex II (COPII) (Hussain et al., 2012). MTP was highly expressed in T-IEL with over 80,000 copies per cell, while less than 100 copies were identified in LN T cells. Similarly, ApoB and the GTPase SAR1b, a key component of the COPII complex, were also expressed in T-IEL at higher copies than in LN T cells (***Figure 5f***). Together, these data suggest that T-IEL also take up and metabolise fatty acids and cholesterol, and further, have the capacity to package these lipids into lipid droplets and potentially even transport them out of the cells.

Intestinal T-IEL proteome contains cell surface receptors for epithelial and neuroimmune interactions

We also explored the expression of proteins uniquely identified in T-IEL and found several proteins involved in cell adhesion, cytoskeleton remodelling and integrin signalling. Strikingly, all T-IEL subsets expressed numerous epithelial cell adhesion molecules and integrins which are not found on naïve LN T cells (***Figure 6a***). Although these results are consistent with the localisation of T-IEL within the gut epithelial layer, we were surprised to find T-IEL proteomes also contained many tight junction, adherens junction and desmosome-associated proteins, which are normally expressed on intestinal epithelial cells, such as E-Cadherin (E-Cad), ZO-2, desmoplakin, Villin-1 and JAM-A (F11R) (***Figure 6a,b***). These proteins could potentially be contaminants from epithelial cells in the sample preparation, however, E-Cad, Occludin and EpCAM have been detected both at the RNA and protein level in T-IEL (***Figure 6- figure supplement 1***, (Inagaki-Ohara et al., 2005; Nochi et al., 2004)). Moreover, immunofluorescence imaging and flow cytometry confirmed expression of ZO-2, E-Cad and EpCAM in T-IEL, suggesting that T-IEL could use these molecules to navigate the tissue environment (***Figure 6c, Figure 6- figure supplement 1***). Conversely, endothelial cell adhesion molecules such as PECAM-1 and L-selectin, that facilitate T cell migration into secondary lymphoid

organs, were highly expressed on naïve T cells, but not on T-IEL, as befits their tissue resident status (***Figure 6d***).

T-IEL proteomes also suggest that T-IEL could be communicating with the enteric nervous system. TCRγδ CD8αα T-IEL express two neural cell adhesion molecules, NCAM1 (CD171) and NrCAM, both implicated in homophilic adhesion and in axonal growth and guidance. Furthermore, two neuropeptide receptors, GPR171 and VIPR2, were also identified in T-IEL proteomes (***Figure 6b***). BigLEN and vasoactive intestinal peptide (VIP) bind to GPR171 and VIPR1/VIPR2, respectively (Delgado et al., 2004; Gomes et al., 2013). BigLEN and VIP are neuropeptides with multiple physiological effects, including gut motility, nutrient absorption, food intake regulation and immune responses (Yoo and Mazmanian, 2017). VIPR2 expression on intestinal innate lymphoid cells was shown to regulate their immune response (Seillet et al., 2020; Talbot et al., 2020). In addition, we also found that T-IEL express GLP1R and GLP2R (***Figure 6b***), receptors for the glucagon-like peptides 1 and 2 (GLP1 and GLP2), which are intestinal peptides involved in regulating appetite and satiety. Both of these receptors were previously mainly found on enteroendocrine cells and enteric neurons. However, recently GLP1R expression on T-IEL was shown to contribute to metabolic syndrome development in mice (He et al., 2019; Yusta et al., 2015). Together, these data suggest that T-IEL may be involved in regulating immune responses and potentially also metabolic responses to food intake through their communication with epithelial cells.

T-IEL share a common signature with exhausted T cells

T-IEL also express many signalling receptors that are absent on naïve T cells and that potentially regulate their poised activated state (Vandereyken et al., 2020). The proteomic analyses here confirmed that all 3 T-IEL subsets express many inhibitory receptors, including LAG-3, CD200R1, CD244 and NK receptors, such as members of the Ly49 family, but also showed that a wider range of these inhibitory receptors are found on innate T-IEL compared to induced T-IEL (***Figure 6b***). Furthermore, T-IEL, regardless of ontogeny, uniformly expressed CD38 and CD73 (*Nt5e*) (***Figures 6b,d***). Indeed, co-expression of CD38 and CD73 is seen to provide a better marker for identifying T-IEL than CD103 expression (***Figure 7a,b***). These receptors are tightly linked to purinergic signalling through their regulation of P2RX7, and as previously found on T_{RM} cells (Borges da Silva et al., 2018; Stark et al., 2018), P2RX7 and CD39 are also highly expressed on T-IEL, although less uniformly than CD38 and CD73 (***Figure 7a,b***).

CD38 and CD39 have recently been identified as markers of T cell exhaustion, along with expression of PD-1, LAG-3, CD244, CD160 among other inhibitory receptors. As all these molecules are highly expressed on T-IEL (***Figure 7a-d***), with the exception of PD-1, T-IEL appear to share some similarities with exhausted T cells (Alfei et al., 2019; Khan et al., 2019; Scott et al., 2019). An overrepresentation analysis using a database of T cell exhaustion markers confirmed that T IEL are enriched in markers of exhaustion (***Figure 7e***), with at least 76 proteins that were upregulated in exhausted T cells also being upregulated in T-IEL (***Figure 7f***, top and ***Supplementary File 5***). During exhaustion of systemic T cells, several proteins are downregulated. Interestingly, a significant proportion of these downregulated proteins are also downregulated in induced T-IEL (***Figure 7f***, bottom and ***Supplementary File 5***). We therefore further examined the expression of transcription factors associated with T cell exhaustion (***Figure 7g***). Indeed, two transcription factors recently identified to be key to imprinting the ‘exhausted’ T cell phenotype, i.e., TOX and

NR4A2, were preferentially expressed in all T-IEL, whereas other transcription factors that show reduced expression in exhausted T cells, including TCF1 and LEF1, were also downregulated in T-IEL. We further confirmed expression of TOX in all T-IEL subsets by flow cytometry (***Figure 7h***). However, T-IEL still express high levels of T-bet, as do effector T cells, which most likely helps to maintain expression of cytolytic effector molecules, such as granzymes, while repressing PD-1 expression on T-IEL. Overall, both natural and induced T-IEL appear to have a hybrid phenotype combining features of exhausted T cells and effector T cells, while also bearing unique hallmarks imprinted by the intestinal microenvironment.

Modifications in the T cell antigen receptor signalosome in T-IEL

Given the connection between T-IEL and exhausted T cells, one key question we wanted to address was whether T-IEL are also unresponsive to TCR stimulation. Indeed, we find that only a small percentage (<10%) of both natural T-IEL subsets are able to respond to TCR crosslinking as measured by induction of phosphorylation of ERK1/2 and S6 ribosomal protein (***Figure 8a,b***). However, induced TCRαβ CD8αβ T-IEL responded even better than LN T cells to TCR stimulation. It has previously been recognised that cross-linking of the TCR on TCRγδ T-IEL does not induce calcium flux and downstream signalling (Malinarich et al., 2010; Wencker et al., 2014). This reduced TCR signalling capacity has been attributed to chronic TCR signalling in the tissue. However, how TCR signalling is dampened at a mechanistic level has not yet been addressed. We sought to evaluate whether there were changes in the TCR signalosome in T-IEL that were blocking TCR signals, and how conserved it was across the different subsets (***Figure 8c***). Strikingly, several proteins were differentially expressed, not just in TCRγδ T-IEL, but in all T-IEL subsets including induced TCRαβ CD8αβ T-IEL. Quantitative analysis of the immediate TCR signalling elements confirmed previous studies showing exclusive expression of FcεR1γ and LAT2 (NTAL/LAB) on T-IEL, and downregulation of LAT and CD3ζ as compared to LN T cells (***Figure 8c***). Replacement of the CD3ζ chain with the FcεR1γ chain reduces the number of immunoreceptor tyrosine-based activation motifs (ITAMs) in the TCR. LAT2 is reported to play a dominant negative role in TCR signalling by competing with LAT for binding partners, but is unable to couple to PLCγ (Fuller et al., 2011).

In addition to LAT and CD3ζ, several other proteins were differentially expressed (***Figure 8c,d***). Surprisingly, many proteins normally found in B cells and involved in BCR signal transduction, were identified as expressed in T-IEL, e.g., Lyn, Syk, LAT2, PLCγ2, Themis2, and many of these are also often found in exhausted T cells (***Supplementary File 5***, (Khan et al., 2019; Schietinger et al., 2016)). We also noted the expression of several negative regulators of TCR signalling, including STS-1 (Ubash3b) that dephosphorylates Zap70/Syk, CD148 (PTPRJ) and DUSP6, which negatively regulates MAPK signalling (Gaud et al., 2018) (***Figure 8c,d***). These negative regulators of signalling are also highly expressed in tumour-associated exhausted T cells (Schietinger et al., 2016). Conversely, key TCR signalling intermediates, such as Protein kinase C θ (PKCθ) and Rac were very poorly expressed. Importantly, many of these changes were not confined to the natural CD8αα T-IEL subsets but were also identified in induced T-IEL.

In summary, these data suggest that the rewiring of the TCR signalosome in T-IEL occurs independently of the developmental pathway through which the 3 different subsets are derived, and is instead shaped by the intestinal environment. However, as induced T-IEL also express LAT2 and FcεR1γ chain, but still respond to

TCR signals, the loss of TCR responsiveness in natural T-IEL cannot be solely attributed to these proteins. Further evaluation of the TCR signalling pathways is necessary to provide an explanation for the loss of TCR responses in natural T-IEL.

Discussion

Both TCRγδ and TCRαβ CD8αα natural T-IEL have long been considered unconventional T cells, due to their unique developmental pathways and their strict restriction to the intestinal epithelium. In contrast, induced T-IEL that arise from systemic antigen-experienced T cells, are considered conventional and more like memory T cells in their ability to respond rapidly to activation signals. Yet our unbiased analyses clearly show that induced T-IEL share far greater similarity to other intestinal T cell subsets than to the systemic T cells they arise from. The T-IEL signature most strikingly contains several proteins thought to be exclusively, or very highly, expressed by enterocytes. These include cognate proteins involved in mediating adherens and tight junction formation, showing that T-IEL are strongly integrated into the intestinal epithelium, by interactions that extend well beyond the CD103: E-cadherin interaction. T-IEL also share metabolic similarities with enterocytes including a strong enrichment in proteins required for cholesterol, lipid and xenobiotic metabolism. Many of these genes are aryl hydrocarbon receptor (AHR) targets (Stockinger et al., 2014; Tanos et al., 2012), suggesting that one reason why AHR is essential for T-IEL survival (Li et al., 2011) is to protect them from toxins and bacterial metabolites in the gut. Other potential indicators of tissue adaptation include expression of the intestine-specific GLUT2 glucose transporter, and the high expression of the urea cycle that could be important for detoxifying the large quantities of ammonia that is present in the intestinal lumen (Romero-Gomez et al., 2009). Furthermore, we find that despite having very low energy requirements, T-IEL have a distinct metabolic signature, with high expression of proteins such as GLUT3, glycerol-3-phosphate shuttle and peroxisomal FAO enzymes. Interestingly, the glycerol phosphate shuttle is normally only expressed in highly glycolytic cells to maintain cellular redox balance by recycling NAD in the cytosol, with most other mammalian cells using the malate-aspartate shuttle for this purpose (Mráček et al., 2013, p.; Spinelli and Haigis, 2018). Thus, we find that T-IEL, far from being metabolically quiescent, have instead a metabolism tailored to their environment, to protect T-IEL from the harsh intestinal environment and actively limit proliferation and activation of these cells.

Ribosomal content was the one area where T-IEL seemed truly deficient in comparison to naïve LN T cells. This was surprising, since naïve T cells, like T-IEL, are not actively cycling cells. However, it was recently shown that a subset of proteins in naïve T cells have short half-lives and are rapidly turned over (Wolf et al., 2020). These included transcription factors that maintain the naïve state, but that need to be rapidly degraded upon T cell activation, allowing T cells to differentiate. Naïve T cells were also found to express a large number of idling ribosomes ready to translate mRNAs required for T cell activation. Thus, the non-existent ribosomal activity in T-IEL subsets is possibly a reflection of their terminally differentiated status. It is also interesting to note that amino acid transporters were expressed at very low levels in T-IEL, thus limiting amino acid availability for protein translation. In this context, we recently showed that activation of T-IEL with IL-15 involves both upregulation of ribosome biogenesis and upregulation of amino acid transporters (James et al., 2020). The low rates of protein translation also highlight the importance of studying the proteome in T-IEL as there may be a significant disconnect between protein and mRNA expression.

In identifying proteins that were expressed solely in T-IEL, but not LN T cells, we uncovered a clear signature of T cell exhaustion within the proteome. Like exhausted T cells, T-IEL have diminished capacity to proliferate in response to TCR triggering, and increased expression of co-inhibitory molecules. However, unlike exhausted T cells, T-IEL maintain high levels of cytotoxic effector molecules, suggesting that they are still capable of killing, although it is unclear what signals are required to trigger full degranulation in T-IEL. Interestingly, despite identifying more than 30 cell surface proteins on T-IEL that were not expressed in LN T cells, no one marker was exclusive to T-IEL, as they were either proteins that were normally expressed in intestinal epithelial cells, or those expressed on activated or exhausted T cells. Thus, the proteomic profiles of T-IEL reveal an interesting mixture of various T cell types; naïve, effector and exhausted, as well their unique tissue-specific signatures.

T-IEL also display several hallmarks of exhausted or suppressed T cells, including a major rewiring of the TCR signalosome. We were surprised to find that LAT2, and many negative regulators of signalling, such as DUSP6 were also expressed in induced T-IEL. These data suggest that the changes in the TCR signalosome are induced by the gut environment, rather than being developmentally regulated. In addition, we found that all T-IEL express ACAT2, a key protein involved in cholesterol esterification, that potentially sequesters cholesterol away from the plasma membrane. Previously, ACAT1, but not the closely related ACAT2, was found to be upregulated in activated $CD8^+$ T cells (Yang et al., 2016). Genetic ablation of ACAT1 lead to increased response from activated T cells in both infection and in cancer, and this was attributed to the increased cholesterol in the plasma membrane leading to increased TCR clustering (Molnár et al., 2012; Yang et al., 2016). Indeed, increased cholesterol content has also been shown to potentiate γδ T cell activation (Cheng et al., 2013). It would be interesting to see if the high levels of ACAT2 expressed in T-IEL prevent accumulation of cholesterol in the T-IEL membranes, thus increasing the activation threshold of T-IEL. On a similar note, ARG2, which was highly expressed in T-IEL, has also been shown to block T cell activation (Geiger et al., 2016; Martí i Líndez et al., 2019), and expression of the alanine metabolizing enzyme, GPT1, may limit alanine availability for protein synthesis in T cell activation (Ron-Harel et al., 2019). Thus, multiple lines of evidence support the notion that both natural and induced T-IEL are tightly regulated through inhibition of signalling.

In summary, we have presented an in-depth proteomic analyses and comparisons of induced and natural T-IEL and systemic T cells. These data provide key insights into the nature of T-IEL as well as the underappreciated similarities between both induced and natural T-IEL. New findings related to cholesterol metabolism, a high energy and translation barrier to activation, and transcription factors that potentially regulate T-IEL function, suggest new ways to investigate how the different T-IEL subsets contribute to tissue and organismal homeostasis.

Acknowledgements

The authors would like to thank Doreen Cantrell for her critical reading of the manuscript, support and advice. We also acknowledge the support provided by A. Whigham and R. Clarke from the Flow Cytometry Facility for cell sorting and flow cytometry, and by the Biological Resources Unit at the University of Dundee. The contribution of the UK Research Partnership Infrastructure Fund award to the Centre for Translational and Interdisciplinary Research for the purchase of the mass spectrometers is gratefully acknowledged.

Competing interests

The authors declare that they have no conflict of interest.

423 **Material and Methods**

Key Resources Table				
Reagent type (species) or resource	**Designation**	**Source or reference**	**Identifiers**	**Additional information**
Genetic reagent (M. musculus)	P14	PMID: 2573841		
Strain, strain background (M. musculus)	C57BL/6J	Charles Rivers	RRID: IMSR_JAX:000664	
Chemical compound, drug	DAPI	Thermo Fisher Scientific	Cat # D1306	1 ug/ml
Antibody	Anti-CD4 (rat, monoclonal)	Thermo Fisher Scientific (eBiosciences)	RRID: AB_494000	cell surface staining (1:200)
Antibody	Anti-CD8a (rat, monoclonal)	Biolegend	RRID: AB_2562558	cell surface staining (1:400)
Antibody	Anti-CD8a (rat, monoclonal)	Biolegend	RRID: AB_312746	immunofluorescence (1:100)
Antibody	Anti-CD8b (rat, monoclonal)	eBioscience	RRID: AB_657764 RRID: AB_1121888	cell surface staining (1:400)
Antibody	Anti-CD38 (rat, monoclonal)	BioLegend	RRID: AB_312928 RRID: AB_312929	Cell surface staining (1:200)
Antibody	Anti-CD39 (rat, monoclonal)	BioLegend	RRID: AB_2563395	Cell surface staining (1:200)
Antibody	Anti-CD44 (rat, monoclonal)	BD Biosciences	RRID: AB_1272244	Cell surface staining (1:200)
Antibody	Anti-CD62L (rat, monoclonal)	Thermo Fisher Scientific	RRID: AB_469632	Cell surface staining (1:200)

Antibody	Anti-CD73 (rat, monoclonal)	BioLegend	RRID: AB_11219608	Cell surface staining (1:200)
Antibody	Anti-CD96 (rat, monoclonal)	BioLegend	RRID: AB_1279389	Cell surface staining (1:200)
Antibody	Anti-CD103 (armenian hamster, monoclonal)	Biolegend	RRID: AB_2563691	Cell surface staining (1:200)
Antibody	Anti-CD160 (rat, monoclonal)	BioLegend	RRID: AB_10960740 RRID: AB_10960743	Cell surface staining (1:200)
Antibody	Anti-CD244 (rat, monoclonal)	eBioscience	RRID: AB_657872	Cell surface staining (1:200)
Antibody	Anti-E-cadherin (mouse monoclonal)	BD Biosciences	RRID: AB_397581	Immunofluorescence (1:100)
Antibody	Anti-LAG-3 (rat, monoclonal)	eBioscience	RRID: AB_2573427	Cell surface staining (1:100)
Antibody	Anti-P2X7R (rat, monoclonal)	BioLegend	RRID: AB_2650951	Cell surface staining (1:200)
Antibody	Anti-TCRb (armenian hamster, monoclonal)	BioLegend	RRID: AB_2629696	Cell surface staining (1:100)
Antibody	Anti-EpCam (rat, monoclonal)	eBioscience	RRID: AB_953617	Cell surface staining (1:200)
Antibody	Anti-E-Cadherin (rat, monoclonal)	eBioscience	RRID: AB_1834417	Cell surface staining (1:100)
Antibody	Anti- TCRγδ (armenian hamster, monoclonal)	BioLegend	RRID: AB_2563356	Cell surface staining (1:200)

Antibody	Anti-phospho S6 (S235/236) (rabbit, monoclonal)	Cell Signaling Technology	RRID: AB_916156	Intracellular staining (1:25)
Antibody	Anti-phospho ERK1/2 (T202/Y204) (rabbit, monoclonal)	Cell Signalling Technology	RRID: AB_331775	Intracellular staining (1:200)
Antibody	Anti-ZO-2 (rabbit polyclonal)	Cell Signaling Technology	RRID: AB_2203575	Immunofluorescence (1:50)
Antibody	Anti-CD3e (armenian hamster, monoclonal)	BioLegend	RRID: AB_312667	TCR stimulation (30ug/ml)
Chemical compound, drug	PP2	Merck (Calbiochem)	Cat # 529573	TCR stimulation, Src inhibitor
Chemical compound , drug	O-Propargyl-puromycin	JenaBioscience	NU-931-05	Protein synthesis measurements
Commercial assay or kit	EasySep CD8+ T cell isolation kit	STEMCELL Technologies, UK	Cat # 19853	For isolating CD8+ T cells from LNs
Commercial assay or kit	EasySep Mouse CD8a Positive Selection Kit II	STEMCELL Technologies, UK	Cat # 18953	For enriching CD8α+ IEL
Commercial assay or kit	EasySep Dead Cell Removal (Annexin V) Kit	STEMCELL Technologies, UK	Cat # 17899	For removing dead epithelial cells and enriching IEL
Commercial assay or kit	Amplex Red cholesterol Assay Kit	Invitrogen	Cat # A12216	Cholesterol assay
Commercial assay or kit	EZQ protein quantification kit	Thermo Fisher Scientific	Cat # R33200	For accurate protein quantification for proteomics

software, algorithm	MaxQuant	https://www.maxquant.org/	RRID:SCR_014485	Version 1.6.3.3
software, algorithm	Limma	Ritchie et al., 2015	RRID: SCR_010943	Version 3.7
software, algorithm	Qvalue	Bioconductor	RRID: SCR_001073	Version 2.10
software, algorithm	FlowJo	Treestar		Version 10
software, algorithm	OMERO.figure	https://pypi.org/project/omero-figure/		Version 4.4.0
Other	RPMI 1640	Thermo Fisher Scientific/GIBCO	21875–034	Media to culture cells

Mice

All mice were bred and maintained with approval by the University of Dundee ethical review committee in compliance with U.K. Home Office Animals (Scientific Procedures) Act 1986 guidelines. C57BL/6J mice were purchased from Charles Rivers and acclimatised for a minimum of 10 days prior to use in experiments. Mice were maintained in a standard barrier facility on a 12hour light/dark cycle at 21ºC, 45-65% relative humidity, in individually ventilated cages with corn cob and sizzler-nest material and fed an R&M3 diet (Special Diet Services, UK) and filtered water ad libitum. Cages were changed at least every two weeks. For all experiments mice were used between 8-12 weeks of age, and for proteomics, male mice aged 8-9 weeks were used.

T-IEL and LN CD8 T cell isolation

T-IEL were isolated for sorting from mice and as described in (James et al., 2020). Briefly, small intestines were extracted and flushed. Small intestines were longitudinally opened, then transversely cut into ~5 mm pieces and put into warm media containing 1mM DTT. Small intestine pieces were shaken for 40min, centrifuged, vortexed and passed through a 100µm sieve. The flow-through was centrifuged on a 36%/67% Percoll density gradient at 700g for 30 minutes. The T-IEL were isolated from the interface between 36% and 67% Percoll. In some experiments, isolated T-IEL were further enriched using an EasySep™ Mouse CD8α positive selection kit (STEMCELL Technologies) as per the manufacturer's instructions. Isolation and sorting details for the LN and effector populations used for proteomics can be found at www.Immpres.co.uk under the 'Protocols & publications' tab.

Proteomics sample preparation and peptide fractionation

Sample preparation was done as in (Howden et al., 2019). Briefly, cell pellets were lysed, boiled and sonicated, and proteins purified using the SP3 method (Hughes et al., 2014). Proteins were digested with LysC and Trypsin and TMT labelling and peptide clean-up performed according to the SP3 protocol. The TMT labelling set up is available in Supplementary File 6. The TMT samples were fractionated using off-line high-pH reverse-phase chromatography: samples were loaded onto a 4.6 mm × 250 mm Xbridge BEH130 C18 column with 3.5 µm particles (Waters). Using a Dionex BioRS system, the samples were separated using a 25-min multistep gradient of solvents A (10 mM formate at pH 9 in 2% acetonitrile) and B (10 mM ammonium formate at pH 9 in 80% acetonitrile), at a flow rate of 1 ml min^{-1}. Peptides were separated into 48 fractions, which were consolidated into 24 fractions. The fractions were subsequently dried, and the peptides were dissolved in 5% formic acid and analysed by liquid chromatography–mass spectrometry.

Liquid chromatography electrospray–tandem mass spectrometry analysis

For each fraction, 1 µg was analysed using an Orbitrap Fusion Tribrid mass spectrometer (Thermo Fisher Scientific) equipped with a Dionex ultra-high-pressure liquid chromatography system (RSLCnano). Reversed-phase liquid chromatography was performed using a Dionex RSLCnano high-performance liquid chromatography system (Thermo Fisher Scientific). Peptides were injected onto a 75 µm × 2 cm PepMap-C18 pre-column and resolved on a 75 µm × 50 cm RP C18 EASY-Spray temperature-controlled integrated column-emitter (Thermo Fisher Scientific) using a 4-h multistep gradient from 5% B to 35% B with a constant flow of 200 nl min^{-1}. The mobile phases were: 2% acetonitrile incorporating 0.1% formic acid (solvent A) and 80% acetonitrile incorporating 0.1% formic acid (solvent B). The spray was initiated by applying 2.5 kV to the EASY-Spray emitter, and the data were acquired under the control of Xcalibur software in a data-dependent mode using the top speed and 4 s duration per cycle. The survey scan was acquired in the Orbitrap covering the *m/z* range from 400–1,400 Thomson units (Th), with a mass resolution of 120,000 and an automatic gain control (AGC) target of 2.0×10^5 ions. The most intense ions were selected for fragmentation using collision-induced dissociation in the ion trap with 30% collision-induced dissociation energy and an isolation window of 1.6 Th. The AGC target was set to 1.0×10^4, with a maximum injection time of 70 ms and a dynamic exclusion of 80 s. During the MS3 analysis for more accurate TMT quantifications, ten fragment ions were co-isolated using synchronous precursor selection, a window of 2 Th and further fragmented using a higher-energy collisional dissociation energy of 55%. The fragments were then analysed in the Orbitrap with a resolution of 60,000. The AGC target was set to 1.0×10^5 and the maximum injection time was set to 300 ms.

MaxQuant processing

The raw proteomics data were analysed with MaxQuant (v. 1.6.3.3) (Cox and Mann, 2008; Tyanova et al., 2016) and searched against a hybrid database. The database contained all murine SwissProt entries, along with TrEMBL entries with a human paralog annotated within human SwissProt and with protein level evidence. The data was searched with the following modifications: carbamidomethylation of cysteine, as well as TMT modification on peptide amino termini and lysine side chains as fixed modifications; methionine oxidation and acetylation of amino termini of proteins were variable modifications. The false discovery rate was set to 1% at the protein and PSM level.

Protein and BioReplicate filtering

Proteins groups marked as 'Contaminants', 'Reverse' or 'Only identified by site' were filtered out. Additionally, proteins detected with less than 2 unique and razor peptides were also filtered out. Within both the TCRαβ CD8αα and TCRαβ CD8αβ T-IEL one replicate (replicate 4) was filtered out from the downstream analysis due to protein content discrepancies. This biorep displayed a 15% reduction in protein content compared to the other 3 replicates within the TCRγδ CD8αα and an increase in protein content of 32% when compared to the remaining 3 replicates within the TCRαβ CD8αβ.

Protein copy numbers and protein content

Protein copy number were estimated from the MS data using the proteomic ruler (Wisniewski et al., 2014) after allocating the summed MS1 intensities to the different experimental conditions according to their fractional MS3 reporter intensities. The protein content was calculated based on copy numbers. The molecular weight (in Da) of each protein was multiplied by the number of copies for the corresponding protein and then divided by N_A (Avogadro's Constant) to yield the individual protein mass in g $cell^{-1}$. The individual masses were converted into picograms and then summed for all proteins to calculate the protein content.

Differential expression and overrepresentation analyses

All fold-changes and P-values for the individual proteins were calculated in R utilising the bioconductor package LIMMA version 3.7. The Q-values provided were generated in R using the "qvalue" package version 2.10.0. All other p-values were calculated using Welch's T-test. For all overrepresentation analyses (ORA) the background was set to the subset of proteins which were identified in either TCRαβ CD8αβ T- IEL or in LN TCRαβ CD8αβ T cells. The Gene Ontology ORAs were done using DAVID (Jiao et al., 2012) and PANTHER (Mi et al., 2019). Two distinct analyses were performed, one for proteins with a p-value <0.001 and fold change greater than or equal to the median plus 1.5 standard deviations and a second one for proteins with a p-value <0.001 and fold change smaller than or equal to the median minus 1.5 standard deviations. The exhaustion ORA was done using WebGestalt (Wang et al., 2017) using the exhaustion markers provided reported within the literature (Khan et al., 2019) as a functional database for the analysis.

Statistical significance thresholds

For the bar and box plots, symbols on bars represent independent biological replicates. For the mass spectrometry derived bar plots and heatmaps ; **= p-value<0.001 and fold change greater than or equal to the median plus 1 standard deviation, ***= p-value <0.0001 and fold change greater than or equal to the median +/- 1.5 standard deviations, based on the differential expression analyses described above. For all plots with non-MS based data, statistical analyses were carried out using R and GraphPad Prism v.8. The exact tests used are described in the figure legends, and p-values <0.05 were considered significant.

Flow cytometry

Cells were stained with titrated concentrations of the following murine monoclonal antibodies: TCRβ [clone H57-597 (BioLegend)], TCRγδ [clone GL3 (BioLegend or eBioscience)], CD4 [clone RM4-5 (BioLegend)], CD8α [clone 53-6.7 (BioLegend)], CD8β [clone H35-17.2 (eBioscience)], CD103 [clone 2E7 (BioLegend)], CD39 [clone Duha59 (BioLegend)], CD73 [clone Ty/11.8 (BioLegend)], CD38 [clone 90 (BioLegend)], P2X7R

[clone 1F11 (BioLegend)], CD244 [clone eBio244F4 (eBioscience)], LAG-3 [(clone eBioC9B7W)], CD160 [clone 7H1 (BioLegend)], CD96 [clone 3.3 (BioLegend)], EpCAM [clone G8.8 (eBioscience)], E-Cadherin [clone DECMA-1 (eBioscience)], TOX [clone TXRX10 (eBioscience)]. All data was acquired on a LSR Fortessa flow cytometer with DIVA software (BD Biosciences). Data were analysed using FlowJo software v10 (TreeStar).

For TCR stimulation, T-IEL and LN T cells were isolated and enriched for CD8+ as described above. T-IEL were stained with Live/Dead fixable Near-IR (ThermoFisher) (1:250) for 10 min prior to stimulation then combined with LN T cells at a 1:1 ratio and resuspended at a concentration of 10^6 cells/ml in RPMI containing 1% FBS, L-Glutamine and Penicillin/Streptomycin. Cells were warmed at 37°C before being stimulated with 30µg/ml of anti-CD3 antibody [clone 145-2C11 (BioLegend)] and 5µg/ml of polyclonal anti-hamster crosslinking antibody (Jackson ImmunoResearch) for 5 min at 37°C. For some samples as indicated, PP2 was added at a concentration of 20µM for 1 hour prior to stimulation. After stimulation cells were directly fixed in 2% PFA 10 min at 37°C before permeabilization with 90% ice cold methanol. Samples were then fluorescently barcoded with different concentration (0, 11.1, 33.3 or 100µg/ml) of the Pacific Blue Dye (ThermoFisher) for 40 min, on ice before quenching with PBS+ 0.5% BSA (v:v). Barcoded samples were then pooled and stained for intracellular phospho-proteins, phospho-p44/42 MAPK (Erk1/2) (Thr202/Tyr204) [Clone 197G2 (Cell Signalling Technologies)] and phospho-S6 ribosomal protein (Ser235/236) [Clone D57.2.2E (Cell Signalling Technologies)] for 30 min at RT, protected from light, followed by secondary DyLight649 antibody (BioLegend). Cells were then stained for surface markers. Data were acquired using CytoFlex flow cytometer and analysed using FlowJo software (v10). Data were analysed using the "Forward deconvolution method" described in (Krutzik and Nolan, 2006). Briefly, samples were differentiated based in the fluorescence intensities of each dye and then individual samples were analysed for their respective phospho-protein expression.

Protein synthesis measurements

For comparing rates of protein synthesis, T-IEL and LN single cell suspensions were cultured with 20µM O-propargyl-puromycin (OPP) (JenaBioscience) for 15 minutes. As a negative control, cells were pre-treated with 0.1mg/mL cycloheximide (CHX) for 15 minutes before adding the OPP for 15 minutes (30m total CHX exposure). Cells were then harvested, fixed with 4% paraformaldehyde (PFA) and permeabilised with 0.5 % triton X-100 before undergoing a copper catalysed click chemistry reaction with Alexa 647-azide (Sigma). Following surface marker staining, cells were resuspended in PBS + 1% BSA and analysed by flow cytometry to determine the degree of incorporation of OPP. All samples were acquired on a LSR Fortessa flow cytometer with DIVA software (BD Biosciences). Data were analysed using FlowJo software.

Cellular cholesterol measurements

Cholesterol content was measured using the Amplex Red cholesterol Assay Kit (Invitrogen). T-IEL were sorted into TCRβ+CD8αα+, TCRβ+CD8αβ+ and TCRγδ+CD8αα+ populations and LN cells were sorted for TCRβ+CD8αβ CD44-lo CD62L-hi cells using the BD Influx Cell Sorter (BD Biosciences). Each population was lysed at a concentration of $10x10^6$ cells/ml in 1X Amplex Red reaction buffer (Invitrogen) for 10 minutes at 4°C then spun at 13,200 rpm for 12 minutes. Lysate was removed and diluted in 1X Amplex Red reaction buffer. 50 µl of 300 µM Amplex Red reagent (containing 2 U/ml horseradish peroxidase, 2 U/ml cholesterol

oxidase and 0.2 U/ml cholesterol esterase) was added to 50 µl of diluted lysate. The reaction was incubated for 30 minutes at 37°C in the dark before reading on the Clariostar microplate reader (BMG Labtech) at excitation wavelength of 530 nm and emission wavelength of 590nm. Cholesterol content in the lysates was calculated with reference to cholesterol standards.

Immunofluorescence and imaging

T-IEL and LN T cells were isolated and enriched for CD8+ as described above. T-IEL were then washed twice in RPMI/10%FBS-containing media and further depleted of contaminating dead cells using EasySep™ Dead Cell Removal (Annexin V) Kit (STEMCELL Technologies) as per manufacturer instructions, for negative enrichment of T-IEL. The purity and viability were checked by flow cytometry with CD8α-APC antibody and DAPI. LN CD8 T cells were at >98% purity, and the IEL were enriched to 60% purity.

$1x10^6$ lymphocytes in PBS were gravity-sedimented onto each 18 mm round coverslip (N1.5) as described (Tsang et al., 2017). Cell were fixed in 3.7% PFA in PBS, pH=7.4, for 10 min at room temperature, washed with PBS, permeabilised with 0.5% Triton X-100 in PBS for 15 min, washed with PBS and blocked with 2% bovine serum albumin and 0.1% Triton X-100 in PBS for 45 min prior to staining with primary antibodies diluted as indicated below in blocking solution, or blocking solution alone, for 1h 45 min at room temperature. Antibodies used were polyclonal rabbit anti-ZO-2 (Cell Signalling Technologies) used at 1:50 dilution, mouse monoclonal anti-E-cadherin (BD Biosciences), used at 1:100 dilution, rat monoclonal anti-CD8α-FITC [clone 53-6.7, (Biolegend), used at 1:100]. After three washes with PBS cells were further incubated with appropriate secondary antibodies diluted 1:500 in blocking solution for 1 h. Secondary antibodies used were goat anti-rat-AlexaFluor488 (Invitrogen); goat anti-mouse-AlexaFluor568 (Invitrogen); donkey anti-rabbit-AlexaFluor647 (Jackson ImmunoResearch). After additional 3 washes with PBS cells were stained with 1 µg/ml DAPI in PBS for 10-15 min, washed with PBS and mounted onto glass slides using ProLong gold antifade reagent (Thermo Fisher Scientific) as a mounting media. Stained cells were imaged using LSM 710 confocal microscope operated by Zen software (Zeiss) with a 63x/1.4NA oil immersion objective. For each image, 7-12 optical sections spanning the entire thickness of the cells were collected. The maximal intensity projections were generated and intensities adjusted in identical manner for all images in OMERO using the OMERO.figure app (Allan et al., 2012).

Data availability

The raw and processed mass spectrometry proteomics data have been deposited to the ProteomeXchange Consortium via the PRIDE partner repository (Perez-Riverol et al., 2019) with the dataset identifier PXD023140 (https://www.ebi.ac.uk/pride/archive/projects/PXD023140/). All other data generated in this study are included within the manuscript and supporting files.

References

Alfei F, Kanev K, Hofmann M, Wu M, Ghoneim HE, Roelli P, Utzschneider DT, von Hoesslin M, Cullen JG, Fan Y, Eisenberg V, Wohlleber D, Steiger K, Merkler D, Delorenzi M, Knolle PA, Cohen CJ, Thimme R, Youngblood B, Zehn D. 2019. TOX reinforces the phenotype and longevity of exhausted T cells in chronic viral infection. *Nature* **571**:265–269. doi:10.1038/s41586-019-1326-9

Allan C, Burel J-M, Moore J, Blackburn C, Linkert M, Loynton S, MacDonald D, Moore WJ, Neves C, Patterson A, Porter M, Tarkowska A, Loranger B, Avondo J, Lagerstedt I, Lianas L, Leo S, Hands K,

606 Hay RT, Patwardhan A, Best C, Kleywegt GJ, Zanetti G, Swedlow JR. 2012. OMERO: flexible,
607 model-driven data management for experimental biology. *Nat Methods* **9**:245–253.
608 doi:10.1038/nmeth.1896
609 Argüello RJ, Combes AJ, Char R, Gigan J-P, Baaziz AI, Bousiquot E, Camosseto V, Samad B, Tsui J, Yan
610 P, Boissonneau S, Figarella-Branger D, Gatti E, Tabouret E, Krummel MF, Pierre P. 2020.
611 SCENITH: A Flow Cytometry-Based Method to Functionally Profile Energy Metabolism with Single-
612 Cell Resolution. *Cell Metabolism* **32**:1063-1075.e7. doi:10.1016/j.cmet.2020.11.007
613 Borges da Silva H, Beura LK, Wang H, Hanse EA, Gore R, Scott MC, Walsh DA, Block KE, Fonseca R, Yan
614 Y, Hippen KL, Blazar BR, Masopust D, Kelekar A, Vulchanova L, Hogquist KA, Jameson SC. 2018.
615 The purinergic receptor P2RX7 directs metabolic fitness of long-lived memory CD8+ T cells. *Nature*
616 **559**:264–268. doi:10.1038/s41586-018-0282-0
617 Cheng H-Y, Wu R, Gebre AK, Hanna RN, Smith DJ, Parks JS, Ley K, Hedrick CC. 2013. Increased
618 Cholesterol Content in Gammadelta (γδ) T Lymphocytes Differentially Regulates Their Activation.
619 *PLOS ONE* **8**:e63746. doi:10.1371/journal.pone.0063746
620 Cox J, Mann M. 2008. MaxQuant enables high peptide identification rates, individualized p.p.b.-range mass
621 accuracies and proteome-wide protein quantification. *Nat Biotechnol* **26**:1367–72.
622 doi:10.1038/nbt.1511
623 Delgado M, Pozo D, Ganea D. 2004. The Significance of Vasoactive Intestinal Peptide in
624 Immunomodulation. *Pharmacol Rev* **56**:249–290.
625 Denning TL, Granger SW, Granger S, Mucida D, Graddy R, Leclercq G, Zhang W, Honey K, Rasmussen JP,
626 Cheroutre H, Rudensky AY, Kronenberg M. 2007. Mouse TCRαβ+CD8αα intraepithelial lymphocytes
627 express genes that down-regulate their antigen reactivity and suppress immune responses. *Journal*
628 *of immunology (Baltimore, Md : 1950)* **178**:4230–4239. doi:10.4049/jimmunol.178.7.4230
629 Di Marco Barros R, Roberts NA, Dart RJ, Vantourout P, Jandke A, Nussbaumer O, Deban L, Cipolat S, Hart
630 R, Iannitto ML, Laing A, Spencer-Dene B, East P, Gibbons D, Irving PM, Pereira P, Steinhoff U,
631 Hayday A. 2016. Epithelia Use Butyrophilin-like Molecules to Shape Organ-Specific γδ T Cell
632 Compartments. *Cell* **167**:203-218.e17. doi:10.1016/j.cell.2016.08.030
633 Fahrer AM, Konigshofer Y, Kerr EM, Ghandour G, Mack DH, Davis MM, Chien Y. 2001. Attributes of γδ
634 intraepithelial lymphocytes as suggested by their transcriptional profile. *Proceedings of the National*
635 *Academy of Sciences of the United States of America* **98**:10261–10266.
636 doi:10.1073/pnas.171320798
637 Frizzell H, Fonseca R, Christo SN, Evrard M, Cruz-Gomez S, Zanluqui NG, von Scheidt B, Freestone D,
638 Park SL, McWilliam HEG, Villadangos JA, Carbone FR, Mackay LK. 2020. Organ-specific isoform
639 selection of fatty acid-binding proteins in tissue-resident lymphocytes. *Sci Immunol* **5**:eaay9283.
640 doi:10.1126/sciimmunol.aay9283
641 Fuller DM, Zhu M, Ou-Yang C-W, Sullivan SA, Zhang W. 2011. A tale of two TRAPs: LAT and LAB in the
642 regulation of lymphocyte development, activation, and autoimmunity. *Immunol Res* **49**:97–108.
643 doi:10.1007/s12026-010-8197-3
644 Gaud G, Lesourne R, Love PE. 2018. Regulatory mechanisms in T cell receptor signalling. *Nat Rev Immunol*
645 **18**:485–497. doi:10.1038/s41577-018-0020-8
646 Geiger R, Rieckmann JC, Wolf T, Basso C, Feng Y, Fuhrer T, Kogadeeva M, Picotti P, Meissner F, Mann M,
647 Zamboni N, Sallusto F, Lanzavecchia A. 2016. L-Arginine Modulates T Cell Metabolism and
648 Enhances Survival and Anti-tumor Activity. *Cell* **167**:829-842.e13. doi:10.1016/j.cell.2016.09.031
649 Geltink RIK, Kyle RL, Pearce EL. 2018. Unraveling the Complex Interplay Between T Cell Metabolism and
650 Function. *Annu Rev Immunol* **36**:461–488. doi:10.1146/annurev-immunol-042617-053019
651 Gomes I, Aryal DK, Wardman JH, Gupta A, Gagnidze K, Rodriguiz RM, Kumar S, Wetsel WC, Pintar JE,
652 Fricker LD, Devi LA. 2013. GPR171 is a hypothalamic G protein-coupled receptor for BigLEN, a
653 neuropeptide involved in feeding. *Proc Natl Acad Sci U S A* **110**:16211–16216.
654 doi:10.1073/pnas.1312938110
655 He S, Kahles F, Rattik S, Nairz M, McAlpine CS, Anzai A, Selgrade D, Fenn AM, Chan CT, Mindur JE, Valet
656 C, Poller WC, Halle L, Rotllan N, Iwamoto Y, Wojtkiewicz GR, Weissleder R, Libby P, Fernández-
657 Hernando C, Drucker DJ, Nahrendorf M, Swirski FK. 2019. Gut intraepithelial T cells calibrate
658 metabolism and accelerate cardiovascular disease. *Nature* **566**:115–119. doi:10.1038/s41586-018-
659 0849-9
660 Howden AJM, Hukelmann JL, Brenes A, Spinelli L, Sinclair LV, Lamond AI, Cantrell DA. 2019. Quantitative
661 analysis of T cell proteomes and environmental sensors during T cell differentiation. *Nat Immunol*
662 **20**:1542–1554. doi:10.1038/s41590-019-0495-x
663 Hughes CS, Foehr S, Garfield DA, Furlong EE, Steinmetz LM, Krijgsveld J. 2014. Ultrasensitive proteome
664 analysis using paramagnetic bead technology. *Mol Syst Biol* **10**:757. doi:10.15252/msb.20145625
665 Hussain MM, Rava P, Walsh M, Rana M, Iqbal J. 2012. Multiple functions of microsomal triglyceride transfer
666 protein. *Nutr Metab (Lond)* **9**:14. doi:10.1186/1743-7075-9-14

667 Inagaki-Ohara K, Sawaguchi A, Suganuma T, Matsuzaki G, Nawa Y. 2005. Intraepithelial lymphocytes
668 express junctional molecules in murine small intestine. *Biochemical and biophysical research*
669 *communications* **331**:977–983. doi:10.1016/j.bbrc.2005.04.025
670 James OJ, Vandereyken M, Swamy M. 2020. Isolation, Characterization, and Culture of Intestinal
671 Intraepithelial Lymphocytes. *Methods in molecular biology (Clifton, NJ)* **2121**:141–152.
672 doi:10.1007/978-1-0716-0338-3_13
673 James OJ, Vandereyken M, Marchingo JM, Singh F, Bray SE, Wilson J, Love AG, Swamy M. 2021. IL-15
674 and PIM kinases direct the metabolic programming of intestinal intraepithelial lymphocytes. *Nat*
675 *Commun* **12**:4290. doi:10.1038/s41467-021-24473-2
676 Jiao X, Sherman BT, Huang DW, Stephens R, Baseler MW, Lane HC, Lempicki RA. 2012. DAVID-WS: a
677 stateful web service to facilitate gene/protein list analysis. *Bioinformatics* **28**:1805–1806.
678 doi:10.1093/bioinformatics/bts251
679 Khan O, Giles JR, McDonald S, Manne S, Ngiow SF, Patel KP, Werner MT, Huang AC, Alexander KA, Wu
680 JE, Attanasio J, Yan P, George SM, Bengsch B, Staupe RP, Donahue G, Xu W, Amaravadi RK, Xu
681 X, Karakousis GC, Mitchell TC, Schuchter LM, Kaye J, Berger SL, Wherry EJ. 2019. TOX
682 transcriptionally and epigenetically programs CD8+ T cell exhaustion. *Nature* **571**:211–218.
683 doi:10.1038/s41586-019-1325-x
684 Konjar Š, Frising UC, Ferreira C, Hinterleitner R, Mayassi T, Zhang Q, Blankenhaus B, Haberman N, Loo Y,
685 Guedes J, Baptista M, Innocentin S, Stange J, Strathdee D, Jabri B, Veldhoen M. 2018.
686 Mitochondria maintain controlled activation state of epithelial-resident T lymphocytes. *Science*
687 *Immunology* **3**:eaan2543. doi:10.1126/sciimmunol.aan2543
688 Li Y, Innocentin S, Withers DR, Roberts NA, Gallagher AR, Grigorieva EF, Wilhelm C, Veldhoen M. 2011.
689 Exogenous stimuli maintain intraepithelial lymphocytes via aryl hydrocarbon receptor activation. *Cell*
690 **147**:629–640. doi:10.1016/j.cell.2011.09.025
691 Ma EH, Verway MJ, Johnson RM, Roy DG, Steadman M, Hayes S, Williams KS, Sheldon RD, Samborska B,
692 Kosinski PA, Kim H, Griss T, Faubert B, Condotta SA, Krawczyk CM, DeBerardinis RJ, Stewart KM,
693 Richer MJ, Chubukov V, Roddy TP, Jones RG. 2019. Metabolic Profiling Using Stable Isotope
694 Tracing Reveals Distinct Patterns of Glucose Utilization by Physiologically Activated $CD8^+$ T Cells.
695 *Immunity* **51**:856-870.e5. doi:10.1016/j.immuni.2019.09.003
696 Madison BB. 2016. Srebp2: A master regulator of sterol and fatty acid synthesis. *Journal of Lipid Research*
697 **57**:333–335. doi:10.1194/jlr.C066712
698 Malinarich FH, Grabski E, Worbs T, Chennupati V, Haas JD, Schmitz S, Candia E, Quera R, Malissen B,
699 Förster R, Hermoso M, Prinz I. 2010. Constant TCR triggering suggests that the TCR expressed on
700 intestinal intraepithelial γδ T cells is functional in vivo. *European Journal of Immunology* **40**:3378–
701 3388. doi:10.1002/eji.201040727
702 Marchingo JM, Sinclair LV, Howden AJ, Cantrell DA. 2020. Quantitative analysis of how Myc controls T cell
703 proteomes and metabolic pathways during T cell activation. *eLife* **9**:e53725. doi:10.7554/eLife.53725
704 Martí i Líndez A-A, Dunand-Sauthier I, Conti M, Gobet F, Núñez N, Hannich JT, Riezman H, Geiger R,
705 Piersigilli A, Hahn K, Lemeille S, Becher B, De Smedt T, Hugues S, Reith W. 2019. Mitochondrial
706 arginase-2 is a cell-autonomous regulator of CD8+ T cell function and antitumor efficacy. *JCI Insight*
707 **4**:132975. doi:10.1172/jci.insight.132975
708 Mi H, Muruganujan A, Huang X, Ebert D, Mills C, Guo X, Thomas PD. 2019. Protocol Update for large-scale
709 genome and gene function analysis with the PANTHER classification system (v.14.0). *Nat Protoc*
710 **14**:703–721. doi:10.1038/s41596-019-0128-8
711 Molnár E, Swamy M, Holzer M, Beck-García K, Worch R, Thiele C, Guigas G, Boye K, Luescher IF, Schwille
712 P, Schubert R, Schamel WWA. 2012. Cholesterol and Sphingomyelin Drive Ligand-independent T-
713 cell Antigen Receptor Nanoclustering. *Journal of Biological Chemistry* **287**:42664–42674.
714 doi:10.1074/jbc.M112.386045
715 Mráček T, Drahota Z, Houštěk J. 2013. The function and the role of the mitochondrial glycerol-3-phosphate
716 dehydrogenase in mammalian tissues. *Biochimica et Biophysica Acta (BBA) - Bioenergetics*
717 **1827**:401–410. doi:10.1016/j.bbabio.2012.11.014
718 Nochi T, Yuki Y, Terahara K, Hino A, Kunisawa J, Kweon M-N, Yamaguchi T, Kiyono H. 2004. Biological role
719 of Ep-CAM in the physical interaction between epithelial cells and lymphocytes in intestinal
720 epithelium. *Clinical immunology (Orlando, Fla)* **113**:326–339. doi:10.1016/j.clim.2004.08.013
721 Olivares-Villagómez D, Van Kaer L. 2018. Intestinal Intraepithelial Lymphocytes: Sentinels of the Mucosal
722 Barrier. *Trends in immunology* **39**:264–275. doi:10.1016/j.it.2017.11.003
723 Pan X, Hussain MM. 2012. Gut triglyceride production. *Biochimica et Biophysica Acta (BBA) - Molecular and*
724 *Cell Biology of Lipids* **1821**:727–735. doi:10.1016/j.bbalip.2011.09.013
725 Pan Y, Tian T, Park CO, Lofftus SY, Mei S, Liu X, Luo C, O'Malley JT, Gehad A, Teague JE, Divito SJ,
726 Fuhlbrigge R, Puigserver P, Krueger JG, Hotamisligil GS, Clark RA, Kupper TS. 2017. Survival of

tissue-resident memory T cells requires exogenous lipid uptake and metabolism. *Nature* **543**:252–256. doi:10.1038/nature21379

Perez-Riverol Y, Csordas A, Bai J, Bernal-Llinares M, Hewapathirana S, Kundu DJ, Inuganti A, Griss J, Mayer G, Eisenacher M, Pérez E, Uszkoreit J, Pfeuffer J, Sachsenberg T, Yilmaz S, Tiwary S, Cox J, Audain E, Walzer M, Jarnuczak AF, Ternent T, Brazma A, Vizcaíno JA. 2019. The PRIDE database and related tools and resources in 2019: improving support for quantification data. *Nucleic Acids Res* **47**:D442–D450. doi:10.1093/nar/gky1106

Romero-Gomez M, Jover M, Galan JJ, Ruiz A. 2009. Gut ammonia production and its modulation. *Metab Brain Dis* **24**:147–57. doi:10.1007/s11011-008-9124-3

Ron-Harel N, Ghergurovich JM, Notarangelo G, LaFleur MW, Tsubosaka Y, Sharpe AH, Rabinowitz JD, Haigis MC. 2019. T Cell Activation Depends on Extracellular Alanine. *Cell Reports* **28**:3011-3021.e4. doi:10.1016/j.celrep.2019.08.034

Sasson SC, Gordon CL, Christo SN, Klenerman P, Mackay LK. 2020. Local heroes or villains: tissue-resident memory T cells in human health and disease. *Cell Mol Immunol* **17**:113–122. doi:10.1038/s41423-019-0359-1

Schietinger A, Philip M, Krisnawan VE, Chiu EY, Delrow JJ, Basom RS, Lauer P, Brockstedt DG, Knoblaugh SE, Hämmerling GJ, Schell TD, Garbi N, Greenberg PD. 2016. Tumor-Specific T Cell Dysfunction Is a Dynamic Antigen-Driven Differentiation Program Initiated Early during Tumorigenesis. *Immunity* **45**:389–401. doi:10.1016/j.immuni.2016.07.011

Scott AC, Dündar F, Zumbo P, Chandran SS, Klebanoff CA, Shakiba M, Trivedi P, Menocal L, Appleby H, Camara S, Zamarin D, Walther T, Snyder A, Femia MR, Comen EA, Wen HY, Hellmann MD, Anandasabapathy N, Liu Y, Altorki NK, Lauer P, Levy O, Glickman MS, Kaye J, Betel D, Philip M, Schietinger A. 2019. TOX is a critical regulator of tumour-specific T cell differentiation. *Nature* **571**:270–274. doi:10.1038/s41586-019-1324-y

Seillet C, Luong K, Tellier J, Jacquelot N, Shen RD, Hickey P, Wimmer VC, Whitehead L, Rogers K, Smyth GK, Garnham AL, Ritchie ME, Belz GT. 2020. The neuropeptide VIP confers anticipatory mucosal immunity by regulating ILC3 activity. *Nat Immunol* **21**:168–177. doi:10.1038/s41590-019-0567-y

Shires J, Theodoridis E, Hayday AC. 2001. Biological insights into TCRgammadelta+ and TCRalphabeta+ intraepithelial lymphocytes provided by serial analysis of gene expression (SAGE). *Immunity* **15**:419–434.

Sinclair LV, Howden AJ, Brenes A, Spinelli L, Hukelmann JL, Macintyre AN, Liu X, Thomson S, Taylor PM, Rathmell JC, Locasale JW, Lamond AI, Cantrell DA. 2019. Antigen receptor control of methionine metabolism in T cells. *eLife* **8**:e44210. doi:10.7554/eLife.44210

Spinelli JB, Haigis MC. 2018. The multifaceted contributions of mitochondria to cellular metabolism. *Nat Cell Biol* **20**:745–754. doi:10.1038/s41556-018-0124-1

Stark R, Wesselink TH, Behr FM, Kragten NAM, Arens R, Koch-Nolte F, van Gisbergen KPJM, van Lier RAW. 2018. **T_{RM} maintenance is regulated by tissue damage via P2RX7**. *Sci Immunol* **3**:eaau1022. doi:10.1126/sciimmunol.aau1022

Stockinger B, Meglio PD, Gialitakis M, Duarte JH. 2014. The Aryl Hydrocarbon Receptor: Multitasking in the Immune System. *Annu Rev Immunol* **32**:403–432. doi:10.1146/annurev-immunol-032713-120245

Talbot J, Hahn P, Kroehling L, Nguyen H, Li D, Littman DR. 2020. Feeding-dependent VIP neuron–ILC3 circuit regulates the intestinal barrier. *Nature* **579**:575–580. doi:10.1038/s41586-020-2039-9

Tanos R, Patel RD, Murray IA, Smith PB, Patterson AD, Perdew GH. 2012. Aryl hydrocarbon receptor regulates the cholesterol biosynthetic pathway in a dioxin response element-independent manner. *Hepatology* **55**:1994–2004. doi:10.1002/hep.25571

Tsang M, Gantchev J, Ghazawi FM, Litvinov IV. 2017. Protocol for adhesion and immunostaining of lymphocytes and other non-adherent cells in culture. *BioTechniques* **63**. doi:10.2144/000114610

Tyanova S, Temu T, Cox J. 2016. The MaxQuant computational platform for mass spectrometry-based shotgun proteomics. *Nat Protoc* **11**:2301–2319. doi:10.1038/nprot.2016.136

Vandereyken M, James OJ, Swamy M. 2020. Mechanisms of activation of innate-like intraepithelial T lymphocytes. *Mucosal Immunology* **13**:721–731. doi:10.1038/s41385-020-0294-6

Wang J, Vasaikar S, Shi Z, Greer M, Zhang B. 2017. WebGestalt 2017: a more comprehensive, powerful, flexible and interactive gene set enrichment analysis toolkit. *Nucleic Acids Research* **45**:W130–W137. doi:10.1093/nar/gkx356

Wencker M, Turchinovich G, Di Marco Barros R, Deban L, Jandke A, Cope A, Hayday AC. 2014. Innate-like T cells straddle innate and adaptive immunity by altering antigen-receptor responsiveness. *Nat Immunol* **15**:80–87. doi:10.1038/ni.2773

Wisniewski JR, Hein MY, Cox J, Mann M. 2014. A “proteomic ruler” for protein copy number and concentration estimation without spike-in standards. *Mol Cell Proteomics* **13**:3497–506. doi:10.1074/mcp.M113.037309

787 Wolf T, Jin W, Zoppi G, Vogel IA, Akhmedov M, Bleck CKE, Beltraminelli T, Rieckmann JC, Ramirez NJ,
788 Benevento M, Notarbartolo S, Bumann D, Meissner F, Grimbacher B, Mann M, Lanzavecchia A,
789 Sallusto F, Kwee I, Geiger R. 2020. Dynamics in protein translation sustaining T cell preparedness.
790 *Nat Immunol* **21**:927–937. doi:10.1038/s41590-020-0714-5
791 Yang W, Bai Y, Xiong Y, Zhang J, Chen S, Zheng X, Meng X, Li L, Wang J, Xu Chenguang, Yan C, Wang L,
792 Chang CCY, Chang T-Y, Zhang T, Zhou P, Song B-L, Liu W, Sun S, Liu X, Li B, Xu Chenqi. 2016.
793 Potentiating the antitumour response of CD8+ T cells by modulating cholesterol metabolism. *Nature*
794 **531**:651–655. doi:10.1038/nature17412
795 Yen C-LE, Nelson DW, Yen M-I. 2015. Intestinal triacylglycerol synthesis in fat absorption and systemic
796 energy metabolism. *Journal of Lipid Research* **56**:489–501. doi:10.1194/jlr.R052902
797 Yoo BB, Mazmanian SK. 2017. The Enteric Network: Interactions between the Immune and Nervous
798 Systems of the Gut. *Immunity* **46**:910–926. doi:10.1016/j.immuni.2017.05.011
799 Yusta B, Baggio LL, Koehler J, Holland D, Cao X, Pinnell LJ, Johnson-Henry KC, Yeung W, Surette MG,
800 Bang KA, Sherman PM, Drucker DJ. 2015. GLP-1 receptor (GLP-1R) agonists modulate enteric
801 immune responses through the intestinal intraepithelial lymphocyte (IEL) GLP-1R. *Diabetes*
802 **64**:db141577-2549. doi:10.2337/db14-1577
803

804

Figure 1: Quantitative proteomic analyses of induced and natural T-IEL subsets

(a) Schematic of the MS based proteomics workflow. The data were acquired at the MS3 level with synchronous precursor selection (see methods). **(b)** Principal component analysis comparing the TMT based estimated protein copy numbers of conventional naive and effector T cells with T-IEL. CTL, Cytotoxic T lymphocytes. **(c)** Bar plot showing the number of proteins identified across all replicates in the 5 populations used for this study. **(d)** Box plot showing the MS based protein content estimation for all replicates used across the 5 populations. **(e)** Principal component analysis comparing the estimated protein copy numbers across conventional naïve LN T cells and T-IEL subsets. **(f-i)** Scatter plot comparing the estimated copy numbers for **(f)** TCRαβ$^+$ CD8αβ$^+$ T-IEL and WT LN TCRαβ CD8αβ T cells, **(g)** TCRαβ$^+$ CD8αβ$^+$ T-IEL and TCRαβ$^+$ CD8αα$^+$ T-IEL, **(h)** TCRαβ$^+$ CD8αβ$^+$ T-IEL and TCRγδ$^+$ CD8αα$^+$ T-IEL, **(i)** WT LN TCRαβ CD8αβ T cells and p14 LN TCRαβ CD8αβ T cells. Pearson correlation coefficient are included within all the scatter plots. The proteomics data displayed on the plots include CTL (n=3 biological replicates), conventional naïve LN T cells (both WT and p14 n=6 biological replicates), TCRαβ$^+$ CD8αβ$^+$ T-IEL and TCRαβ$^+$ CD8αα$^+$ T-IEL (n=3 biological replicates) and TCRγδ$^+$ CD8αα$^+$ T-IEL (n= 4 biological replicates). For boxplots, the bottom and top hinges represent the 1st and 3rd quartiles. The top whisker extends from the hinge to the largest value no further than 1.5 × IQR from the hinge; the bottom whisker extends from the hinge to the smallest value at most 1.5 × IQR of the hinge. The bar plots show the mean. Total number of proteins identified and total protein content across all populations are available in Figure 1-source data 1.

Figure 1- source data 1: Total protein identifications and total protein content across all populations

Figure 1- figure supplement 1. Gating strategy used to identify and isolate T-IEL subsets using fluorescence activated cell sorting (FACS). Lymphocytes were gated by size using forward scatter (FCS) and side scatter (SSC) and T-IEL subsets were separated based on the cell surface marker expression of T cell-associated receptors: TCRβ, TCRγδ, CD8α, CD8β and CD4. The populations sorted were as followed: cells positive for TCRγδ and CD8αα (TCRγδ CD8αα T-IEL), and those that were both TCRβ+ and CD4- and either CD8αα (TCRβ CD8αα T-IEL) or CD8β (TCRβ CD8αβ T-IEL).

Figure 2: Gene ontology analyses of the induced T-IEL proteome

(a) Treemap showing the abundance of proteins classified into histones, ribosomal proteins, cytoskeletal proteins, glycolytic enzymes, chaperones and granzymes across WT LN TCRαβ CD8αβ T cells and TCRαβ$^+$ CD8αβ$^+$ T-IEL. Rectangle size is proportional to the median estimated copy numbers. Median copy numbers across all categories are available in Figure 2-source data 1. **(b)** Bar plots showing the estimated copy numbers for all granzymes across WT LN TCRαβ CD8αβ T cells (n=6) and all T-IEL (n=3 or 4). Symbols on the bars represent the biological replicates. The bars show the mean and SEM. p-values have been calculated on R with LIMMA where **= p <0.001 and fold change greater than or equal to the median plus 1 standard deviation, ***= p <0.0001 and fold change greater than or equal to the median +/- 1.5 standard deviations. **(c)** Bar plot showing the results of the DAVID functional annotation clustering (FDR<0.05; see methods for details) enrichment analysis for all proteins exclusive to or significantly increased in expression within TCRαβ$^+$ CD8αβ$^+$ T-IEL. **(d)** Bar plot showing the results of the PANTHER GO Biological process (FDR<0.05; see methods for details) enrichment analysis for all proteins exclusive to or significantly increased in expression within TCRαβ$^+$ CD8αβ$^+$ T-IEL (blue) or within WT TCRαβ CD8αβ T cells (red).

Figure 2-source data 1: Median copy numbers for the global analysis

Figure 3: Downregulation of protein synthesis in T-IEL

(a) Box plots showing the estimated total cytoplasmic (left) and mitochondrial (right) ribosomal protein copies for LN TCRβ CD8αβ T cells and all T-IEL subsets. The sums of all copy numbers are available in Figure 3-source data 1. **(b)** Box plots showing the estimated summed total protein copies for the protein subunits that are exclusive to RNA Polymerases I, II and III, respectively for LN TCRβ CD8αβ T cells and all T-IEL subsets. The sum of all copy numbers are available in Figure 3-source data 1. **(c)** Bar plots showing the estimated protein copy numbers of the amino acid transporters, SLC7A5 and SLC38A2, for WT LN TCRβ CD8αβ and all 3 subsets of T-IEL. **(d)** Bar plots showing the estimated protein copy numbers of Arginase 2 (ARG2; left) and alanine aminotransferase (GPT; right) for WT LN TCRβ CD8αβ and all 3 subsets of T-IEL. **(e)** Bar plots showing the estimated protein copy numbers of PRKR-Like Endoplasmic Reticulum Kinase (PERK) for WT LN TCRβ CD8αβ and all 3 T-IEL subsets. **(f)** Bar plots showing the OP-Puromycin (OPP) incorporation (n= 3 biological replicates) in *ex vivo* WT LN TCRβ CD8αβ and T-IEL. As a negative control, OPP incorporation was inhibited by cycloheximide (CHX) pre-treatment. OPP incorporation was assessed by flow cytometry 15 min after administration. Bar graph represents the geometric MFI of the OPP-AlexaFluor 647 in each T cell subsets normalized to the geometric MFI of the CHX pre-treated T cells. p-values were calculated using ordinary one-way ANOVA with Dunnett's multiple comparisons. For all box plots, the bottom and top hinges represent the 1^{st} and 3^{rd} quartiles. The top whisker extends from the hinge to the largest value no further than 1.5 × IQR from the hinge; the bottom whisker extends from the hinge to the smallest value at most 1.5 × IQR of the hinge. All bar plots show the mean and SEM. Symbols on the bars represent the biological replicates. The proteomics data displayed on the plots include WT TCRαβ CD8αβ T cells (n=6 biological replicates), TCRαβ$^+$ CD8αβ$^+$ T-IEL and TCRαβ$^+$ CD8αα$^+$ T-IEL (n=3 biological replicates) and TCRγδ$^+$ CD8αα$^+$ T-IEL (n= 4 biological replicates). The P-values for individual proteins (c,d,e) were calculated in R with LIMMA, where **= p <0.001 and fold change greater than or equal to the median plus 1 standard deviation, ***= p <0.0001 and fold change greater than or equal to the median +/- 1.5 standard deviations, and in (a,b) in R with Welch's T test.

Figure 3-source data 1: Sum of median copy numbers for the cytoplasmic and mitochondrial ribosomes

Figure 3- figure supplement 1: (a) Box plots showing the median Log_2 fold change (T-IEL/LN CD8 T cells) for RNA Polymerase 1, 2 and 3 complexes. Each grey dot represents one of the polymerase subunits. P-values were calculated using one-sample t-tests, where *= p<0.05, **=p<0.01, ***=p<0.001, ns= not significant. **(b)** Schematic representation of the urea cycle. Coloured heatmap squares represent protein expression Log_2 fold change (T-IEL/LN CD8 T cells) in, from left to right, T-IEL TCRβ CD8αβ, T-IEL TCRβ CD8αα and T-IEL TCRγδ CD8αα. Proteins expressed only by T-IEL are highlighted by red squares, representing estimated protein copy numbers (mean from at least 3 biological replicates). For protein names, see supplementary Table 4.

Figure 4: Metabolic profiling of the T-IEL proteome

(a) Stacked bar plots comparing the proportional representation of metabolic pathways in LN TCRβ CD8αβ and all T-IEL subsets. **(b)** Bar plots showing the estimated protein copy numbers of the glucose transporters,

GLUT1, GLUT2 and GLUT3, for WT LN TCRβ CD8αβ and all 3 subsets of T-IEL. **(c)** Heatmaps displaying the Log_2 fold change (T-IEL/ LN CD8 T cells) for all proteins involved in glycolysis, tricarboxylic acid cycle (TCA cycle) and fatty acid oxidation (FAO). **(d)** Bar plots showing the sum of the estimated protein copy numbers of the electron transporter chain (ETC) components, for WT LN TCRβ CD8αβ and all 3 subsets of T-IEL. Sum of the copy numbers across all ETC complexes are available in Figure 4-source data 1. **(e)** Schematic representation of the glycerol 3-phosphate shuttle with heatmaps showing protein expression of cytosolic glycerol-3-phosphate dehydrogenase (cGpDH) and the Log_2 fold change of mitochondrial glycerol-3-phosphate dehydrogenase (mGpDH) (T-IEL/LN CD8 T cells) in, from left to right, T-IEL TCRβ CD8αβ, T-IEL TCRβ CD8αα and T-IEL TCRγδ CD8αα. All bar plots show the mean and SEM. Symbols on the bars represent the biological replicates. The proteomics data displayed on the plots include WT TCRαβ CD8αβ T cells (n=6 biological replicates), $TCR\alpha\beta^+$ $CD8\alpha\beta^+$ T-IEL and $TCR\alpha\beta^+$ $CD8\alpha\alpha^+$ T-IEL (n=3 biological replicates) and $TCR\gamma\delta^+$ $CD8\alpha\alpha^+$ T-IEL (n= 4 biological replicates). P-values for individual proteins (b-c) were calculated in R with LIMMA, where **= p <0.001 and fold change greater than or equal to the median plus 1 standard deviation, ***= p <0.0001 and fold change greater than or equal to the median +/- 1.5 standard deviations, and in (d) in R with Welch's T test. For full protein names, see Supplementary File 4.

Figure 4-source data 1: Sum of median copy numbers for the all the ETC complexes

Figure 5: T-IEL have enhanced cholesterol and lipid metabolism

(a) Schematic representation of proteins involved of the cholesterol biosynthetic pathway. Heatmap squares represent the Log_2 fold change (T-IEL/LN CD8 T cells) in, from left to right, T-IEL TCRβ CD8αβ, T-IEL TCRβ CD8αα and T-IEL TCRγδ CD8αα. Proteins expressed only by T-IEL are highlighted by red squares, representing the mean estimated protein copy numbers (from at least 3 biological replicates). **(b)** Bar plot showing the estimated protein copy number of SREBP2 for WT LN TCRβ CD8αβ and all 3 subsets of T-IEL. **(c)** Bar plot showing a comparison of total cellular cholesterol content in sorted WT LN TCRβ CD8αβ and all 3 subsets of T-IEL (n=4 biological replicates). P-values calculated using ordinary one-way ANOVA with Dunnett's multiple comparison test. Data for the total cholesterol content are available in Figure 5-source data 1. **(d)** Bar plots showing the estimated protein copy numbers of the fatty acid transporters FATP1, FATP2 and FATP4 for WT LN TCRβ CD8αβ and all 3 subsets of T-IEL. **(e)** Bar plots showing the estimated protein copy numbers of the fatty acid binding proteins FABP1, FABP2, FABP5 and FABP6 for WT LN TCRβ CD8αβ and all 3 subsets of T-IEL. **(f)** Schematic representation of the triacylglycerol synthesis pathways and lipoprotein assembly. Coloured squares represent the Log_2 fold change (T-IEL/LN CD8 T cells) in, from left to right, T-IEL TCRβ CD8αβ, T-IEL TCRβ CD8αα and T-IEL TCRγδ CD8αα. Proteins expressed only by T-IEL are highlighted by red squares, representing estimated protein copy numbers (mean from at least 3 biological replicates).

All bar plots show the mean and SEM. Symbols on the bars represent the biological replicates. The proteomics data displayed on the plots include WT TCRαβ CD8αβ T cells (n=6 biological replicates), $TCR\alpha\beta^+$ $CD8\alpha\beta^+$ T-IEL and $TCR\alpha\beta^+$ $CD8\alpha\alpha^+$ T-IEL (n=3 biological replicates) and $TCR\gamma\delta^+$ $CD8\alpha\alpha^+$ T-IEL (n= 4 biological replicates). P-values for individual proteins (a,b,d,e,f) were calculated in R with LIMMA, where **= p <0.001 and fold change greater than or equal to the median plus 1 standard deviation, ***= p <0.0001

and fold change greater than or equal to the median +/- 1.5 standard deviations. For full protein names, see Supplementary File 4.

Figure 5-source data 1: Total cholesterol content across all populations

Figure 6: Cell surface proteins expressed on T-IEL

(a) Schematic representation of proteins involved in cell-cell adhesion that are only expressed by the different T-IEL subsets. **(b)** Heatmaps displaying the estimated protein copy numbers of adhesion molecules, co-signalling receptors, neuropeptide receptors and purinergic receptors expressed only by T-IEL. Data represent the mean of at least 3 biological replicates. **(c)** Purified LN CD8 T cells (left) and isolated T-IEL (right) were immunostained for ZO-2 (top, red), E-cadherin (bottom, green) and CD8α (not shown) and counterstained with DAPI to mark the nuclei (blue). Representative (of 2 independent experiments) maximal intensity projections of confocal sections spanning the entire cell thickness of selected CD8+ cells of each type are shown. Size bars = 2 µm. See also Supplementary Figure 3. **(d)** Heatmap displaying Log_2 fold change (T-IEL/ LN CD8 T) cells of adhesion molecules, co-signalling receptors and purinergic receptors. The proteomics data displayed on the plots show the mean values and were calculated from WT TCRαβ CD8αβ T cells (n=6 biological replicates), TCRαβ$^+$ CD8αβ$^+$ T-IEL and TCRαβ$^+$ CD8αα$^+$ T-IEL (n=3 biological replicates) and TCRγδ$^+$ CD8αα$^+$ T-IEL (n= 4 biological replicates). P-values were calculated in R with LIMMA, where **= p <0.001 and fold change greater than or equal to the median plus 1 standard deviation, ***= p <0.0001 and fold change greater than or equal to the median +/- 1.5 standard deviations.

Figure 6- figure supplement 1: Expression of epithelial proteins in T-IEL. a) Bar plots showing the ImmGen microarray database (www.immgen.org) derived normalised RMA values for *Tjp2* (ZO2), *EpCam* and *Cdh1* (E-Cadherin) across WT naïve CD8 T cells (T.8Nve.Sp and T.8Nve.LN) and TCRγδ Vγ5-ve or Vγ5+ve IEL (Tg.dVg5-.IEL, TgdVg5+IEL) **(b-c)** Comparison, by flow cytometry of the expression of EpCam **(b)** and E-Cadherin **(c)** in WT LN CD8 T cells, all 3 subsets of T-IEL and intestinal epithelial cells (IEC). Bar plots presenting geometric mean fluorescence intensities of n=3 biological replicates are shown on the side of each histogram. Mean ± SEM shown. p-values were calculated using one-way ANOVA and Dunnett's multiple comparisons test. **(d)** Gating strategy used to identify T-IEL and IEC for (b-c). Lymphocytes and IEC were gated by size using forward scatter (FCS) and side scatter (SSC) and doublets were excluded. T-IEL subsets were separated as described in the FACS sorting strategy in supplementary Figure 1. **(e)** ZO-2 and E-cadherin immunofluorescence of IEL and WT LN CD8 T cells. Isolated IEL depleted of Annexin V-positive contaminants (IEL, top) and isolated purified LN CD8 T cells (LN, bottom) were fixed, permeabilised, immunostained for ZO-2 (green on overlay, left panels), E-cadherin (red on overlay, left panels) and CD8α (not shown) or with secondary antibodies only (right panels), and counterstained with DAPI to mark the nuclei (blue). Representative maximal intensity projections of confocal sections spanning the entire cell thickness of CD8α-positive cells of each type are shown. Black and white images show individual ZO-2 (middle rows) or E-cadherin (bottom rows) staining or matching secondary antibody-only controls. All images were acquired and processed identically. Size bars are 2 µm.

Figure 7: T-IEL share similarities with exhausted T cells

(a) Flow cytometry dot plots comparing the expression of purinergic receptors (CD38/CD73, top and P2X7R/CD39, bottom) in WT LN TCRβ CD8αβ and all 3 subsets of T-IEL. **(b)** Stacked doughnut plot showing the percentages of cells from LN CD8 T cells and T-IEL expressing the indicated purinergic receptors, quantified by flow cytometry (n=1 biological replicate). **(c)** Flow cytometric histograms comparing the protein expression of the exhaustion markers, CD244, LAG-3, CD160 and CD96 in all 3 subsets of T-IEL. **(d)** Stacked doughnut plot showing the percentage of cell from LN CD8 T cells and T-IEL expressing the indicated exhaustion markers quantified by flow cytometry (n= 4 biological replicates). **(e)** Bar plot showing the result of the T cells exhaustion overrepresentation analyses in LN TCRβ CD8αβ and in TCRβ CD8αβ T-IEL. **(f)** Venn diagrams showing the commonality of proteins upregulated (top) and downregulated (bottom) during exhaustion and in TCRβ CD8αβ T-IEL. **(g)** Heatmap displaying the Log_2 fold change (T-IEL/LN CD8 T cells) of transcription factors associated with exhaustion in T cells. **(h)** Bar plots showing the estimated protein copy number of TOX (left) and flow cytometry derived MFI for TOX (right) for WT LN TCRβ CD8αβ and all 3 subsets of T-IEL. The proteomics data displayed on the plots include WT TCRαβ CD8αβ T cells (n=6 biological replicates), TCRαβ$^+$ CD8αβ$^+$ T-IEL and TCRαβ$^+$ CD8αα$^+$ T-IEL (n=3 biological replicates) and TCRγδ$^+$ CD8αα$^+$ T-IEL (n= 4 biological replicates). The flow cytometry was performed on 3 biological replicates, representative of 2 independent experiments. P-values for individual proteins (g-h) were calculated in R with LIMMA where **= p <0.001 and fold change greater than or equal to the median plus 1 standard deviation, ***= p <0.0001 and fold change greater than or equal to the median +/- 1.5 standard deviations, for the flow cytometry data (h) in GraphPad prism using one-way ANOVA with Dunnett's multiple comparisons test. For full protein names, see Supplementary File 4.

Figure 7-source data 1: Flow cytometry-based percentage of cells expressing exhaustion markers and TOX MFI

Figure 8: Rewiring of the TCR signalosome in T-IEL

(a-b) Responses of WT LN CD8 T cells and T-IEL to TCR stimulation. Bar plots show the percentage of cells positive for **(a)** phospho-ERK1/2 (T202/Y204) and **(b)** phospho-S6 (S235/236) before and after anti-CD3 stimulation. The Src kinase inhibitor PP2 was added as a control to show that induction of ERK1/2 and S6 phosphorylation was specific. N=3 biological replicates, p-values were calculated by two-way ANOVA with Dunnett's multiple comparisons test. Data are available in Figure 8-source data 1. **(c-d)** Schematic representation of the main TCR signalling pathways comparing the expression of selected proteins in T-IEL and LN naïve T cells. **(c)** TCR and LAT signalosome. **(d)** signalling pathways downstream TCR receptor. All heatmap squares represent the Log_2 fold change (T-IEL/LN CD8 T cells) in, from left to right, T-IEL TCRβ CD8αβ, T-IEL TCRβ CD8αα and T-IEL TCRγδ CD8αα. Proteins expressed only by T-IEL are highlighted by red squares, representing estimated protein copy numbers (mean from at least 3 biological replicates). The proteomics data displayed on the plots was calculated from WT TCRαβ CD8αβ T cells (n=6 biological replicates), TCRαβ$^+$ CD8αβ$^+$ T-IEL and TCRαβ$^+$ CD8αα$^+$ T-IEL (n=3 biological replicates) and TCRγδ$^+$ CD8αα$^+$ T-IEL (n= 4 biological replicates). P-values were calculated in R with LIMMA, where **= p <0.001 and fold change greater than or equal to the median plus 1 standard deviation, ***= p <0.0001 and fold

change greater than or equal to the median +/- 1.5 standard deviations. For protein names, see Supplementary File 4.

Figure 8-source data 1: Flow cytometry-based percentage of cells positive for Phospho ERK1/2 and phospho S6

Supplementary File 1: Estimated protein copy numbers and differential expression analysis derived from the mass spectrometric proteomics data for the 3 T-IEL subsets and WT and P14 LN T cells.

Supplementary File 2: PANTHER Gene Ontology enrichment analysis

Supplementary File 3: DAVID functional annotation enrichment analysis

Supplementary File 4 (related to Figure 4-8): Abbreviations and full protein names of proteins mentioned in the text and figures.

Supplementary File 5 (related to Figure 7e-f)**:** Proteins expressed in induced T-IEL and found to be overrepresented in exhausted T cells gene set, and proteins missing or downregulated in induced T-IEL, found to be underrepresented in exhausted T cells gene set (Khan et al, 2019).

Supplementary File 6: Set up of TMT labelling of samples for proteomics

Figure 1

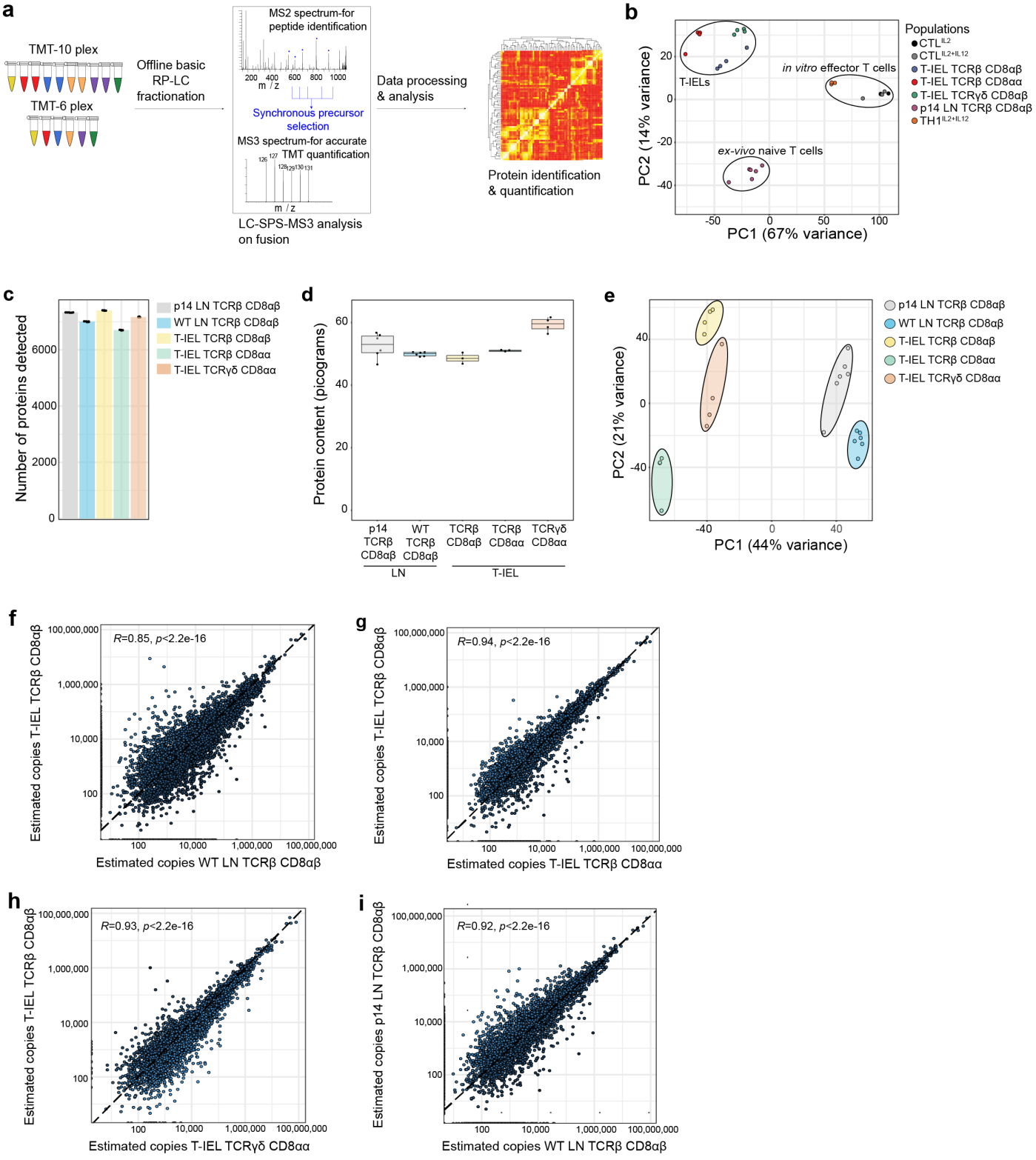
a
TMT-10 plex
TMT-6 plex
Offline basic RP-LC fractionation
MS2 spectrum-for peptide identification
Synchronous precursor selection
MS3 spectrum-for accurate TMT quantification
LC-SPS-MS3 analysis on fusion
Data processing & analysis
Protein identification & quantification
b
Populations
CTL IL2
CTL IL2+IL12
T-IEL TCRβ CD8αβ
T-IEL TCRβ CD8αα
T-IEL TCRγδ CD8αβ
p14 LN TCRβ CD8αβ
TH1 IL2+IL12
T-IELs
in vitro effector T cells
ex-vivo naive T cells
PC2 (14% variance)
PC1 (67% variance)
c
Number of proteins detected
p14 LN TCRβ CD8αβ
WT LN TCRβ CD8αβ
T-IEL TCRβ CD8αβ
T-IEL TCRβ CD8αα
T-IEL TCRγδ CD8αα
d
Protein content (picograms)
p14 TCRβ CD8αβ
WT TCRβ CD8αβ
TCRβ CD8αβ
TCRβ CD8αα
TCRγδ CD8αα
LN
T-IEL
e
PC2 (21% variance)
PC1 (44% variance)
f
R=0.85, p<2.2e-16
Estimated copies T-IEL TCRβ CD8αβ
Estimated copies WT LN TCRβ CD8αβ
g
R=0.94, p<2.2e-16
Estimated copies T-IEL TCRβ CD8αβ
Estimated copies T-IEL TCRβ CD8αα
h
R=0.93, p<2.2e-16
Estimated copies T-IEL TCRβ CD8αβ
Estimated copies T-IEL TCRγδ CD8αα
i
R=0.92, p<2.2e-16
Estimated copies p14 LN TCRβ CD8αβ
Estimated copies WT LN TCRβ CD8αβ

Figure 1- figure supplement 1

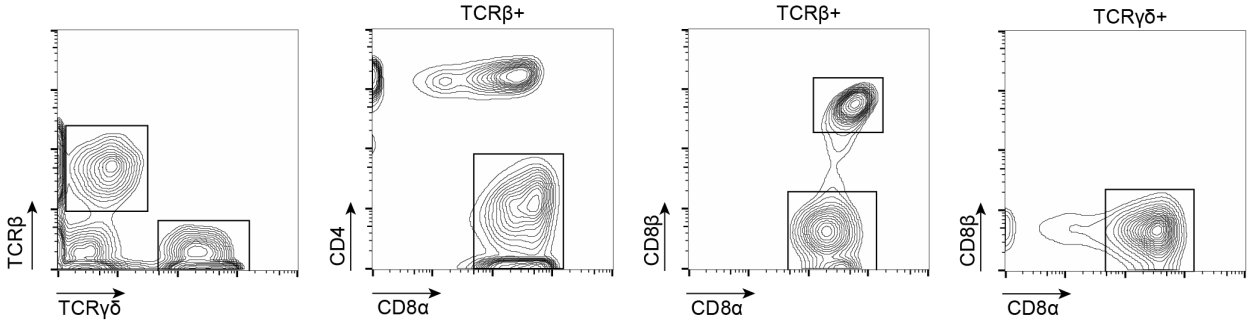

Figure 2

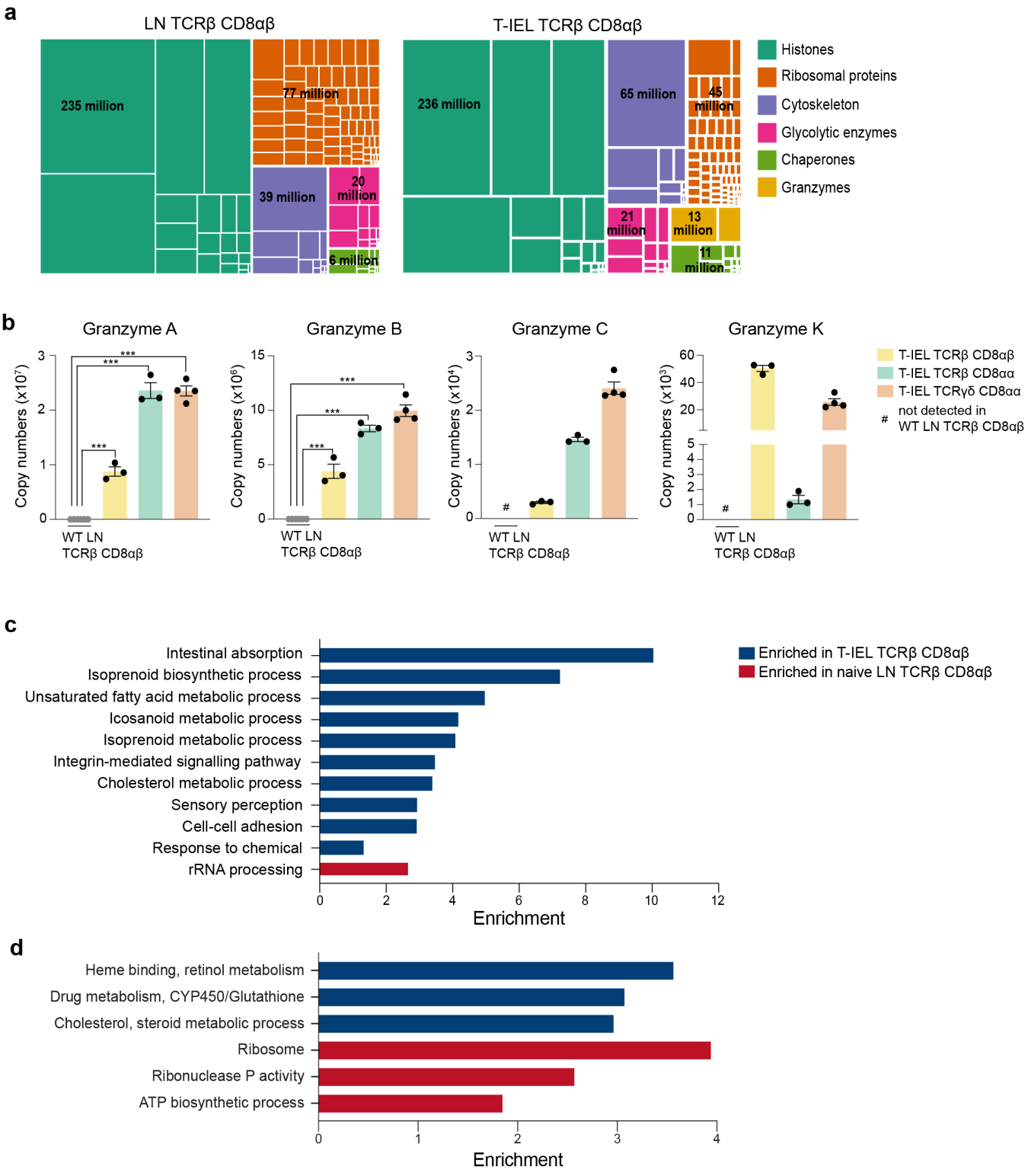
a
LN TCRβ CD8αβ
T-IEL TCRβ CD8αβ
235 million
77 million
39 million
20 million
6 million
236 million
65 million
45 million
21 million
13 million
11 million
Histones
Ribosomal proteins
Cytoskeleton
Glycolytic enzymes
Chaperones
Granzymes
b
Granzyme A
Granzyme B
Granzyme C
Granzyme K
Copy numbers (x10⁷)
Copy numbers (x10⁶)
Copy numbers (x10⁴)
Copy numbers (x10³)
WT LN TCRβ CD8αβ
T-IEL TCRβ CD8αβ
T-IEL TCRβ CD8αα
T-IEL TCRγδ CD8αα
not detected in WT LN TCRβ CD8αβ
c
Intestinal absorption
Isoprenoid biosynthetic process
Unsaturated fatty acid metabolic process
Icosanoid metabolic process
Isoprenoid metabolic process
Integrin-mediated signalling pathway
Cholesterol metabolic process
Sensory perception
Cell-cell adhesion
Response to chemical
rRNA processing
Enrichment
Enriched in T-IEL TCRβ CD8αβ
Enriched in naive LN TCRβ CD8αβ
d
Heme binding, retinol metabolism
Drug metabolism, CYP450/Glutathione
Cholesterol, steroid metabolic process
Ribosome
Ribonuclease P activity
ATP biosynthetic process
Enrichment

Figure 3

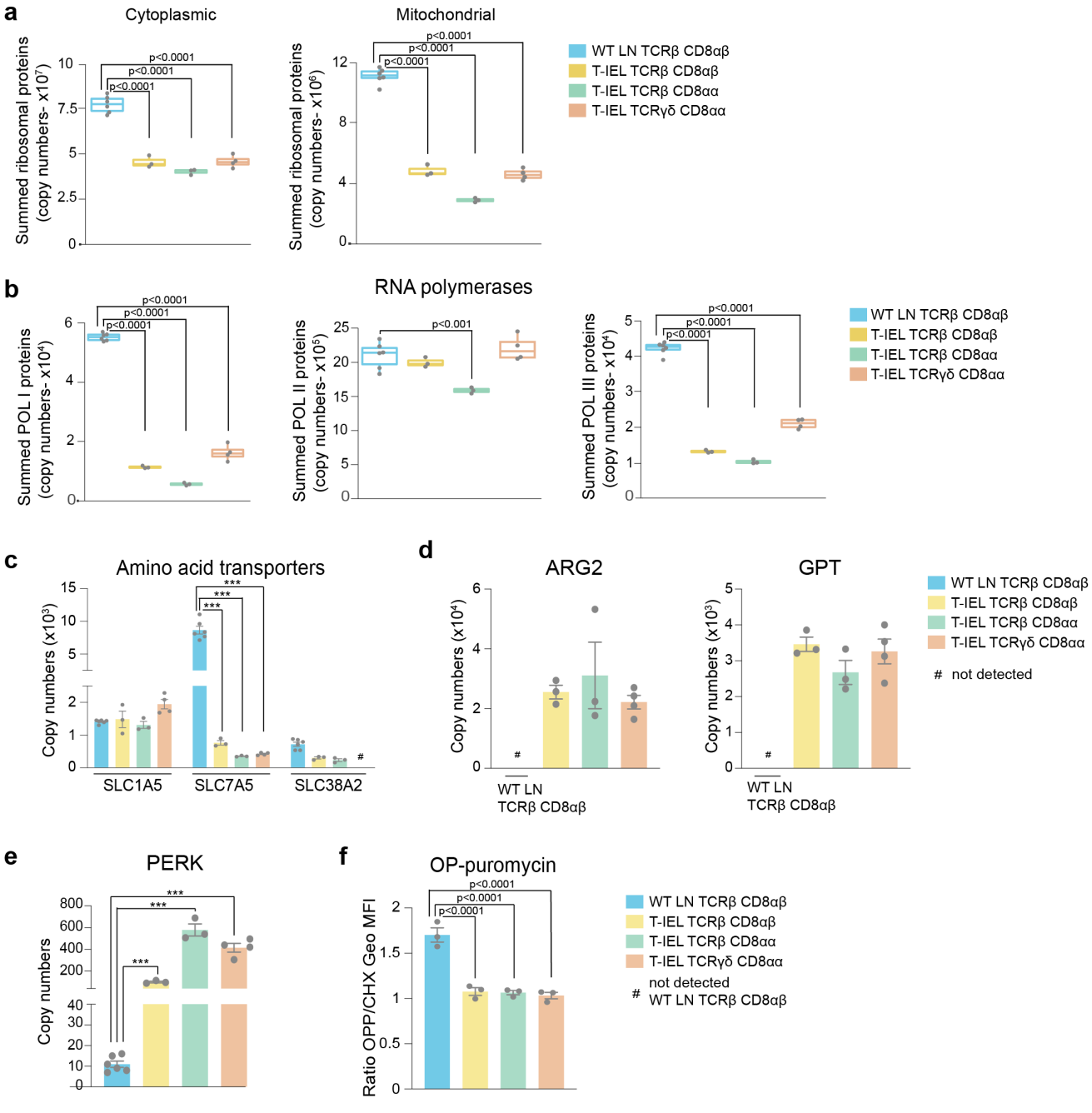
a
Cytoplasmic
Mitochondrial
Summed ribosomal proteins (copy numbers- x10^7)
Summed ribosomal proteins (copy numbers- x10^6)
p<0.0001
WT LN TCRβ CD8αβ
T-IEL TCRβ CD8αβ
T-IEL TCRβ CD8αα
T-IEL TCRγδ CD8αα
b
RNA polymerases
Summed POL I proteins (copy numbers- x10^4)
Summed POL II proteins (copy numbers- x10^5)
Summed POL III proteins (copy numbers- x10^4)
p<0.001
c
Amino acid transporters
Copy numbers (x10^3)
SLC1A5
SLC7A5
SLC38A2
d
ARG2
GPT
Copy numbers (x10^4)
Copy numbers (x10^3)
WT LN TCRβ CD8αβ
not detected
e
PERK
Copy numbers
f
OP-puromycin
Ratio OPP/CHX Geo MFI
not detected
WT LN TCRβ CD8αβ

Figure 3-figure supplement 1

a

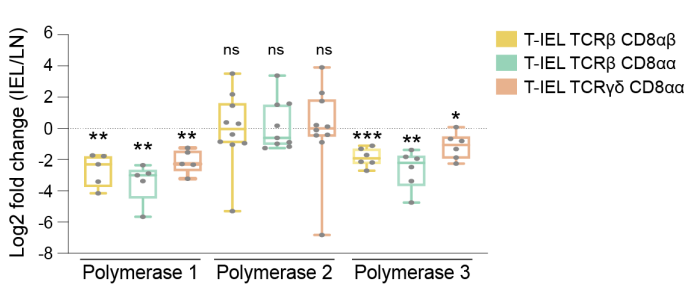

b

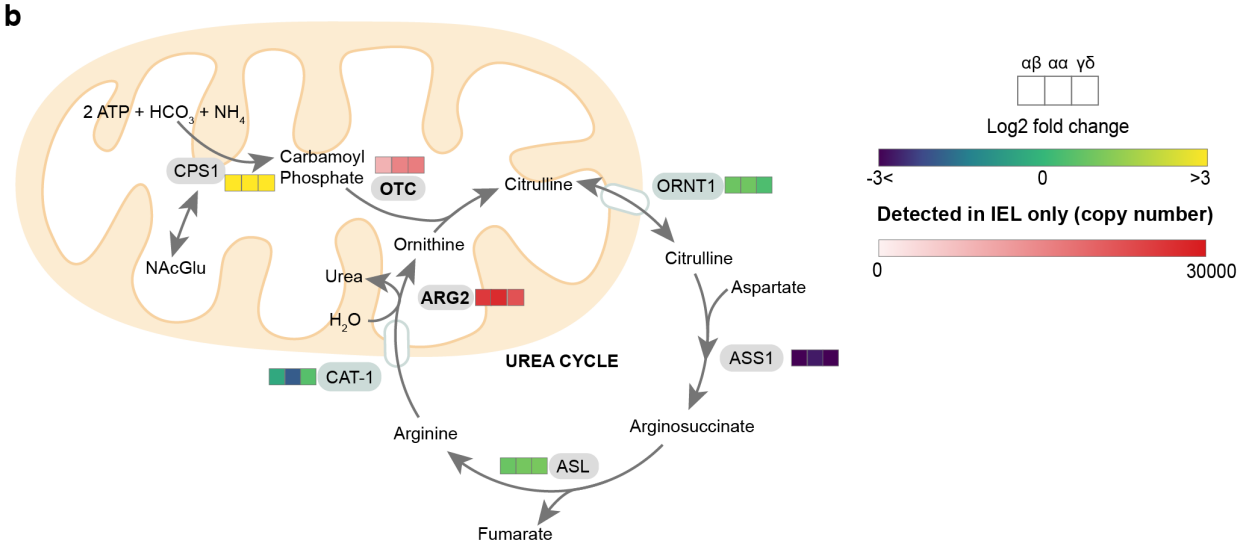

Figure 4

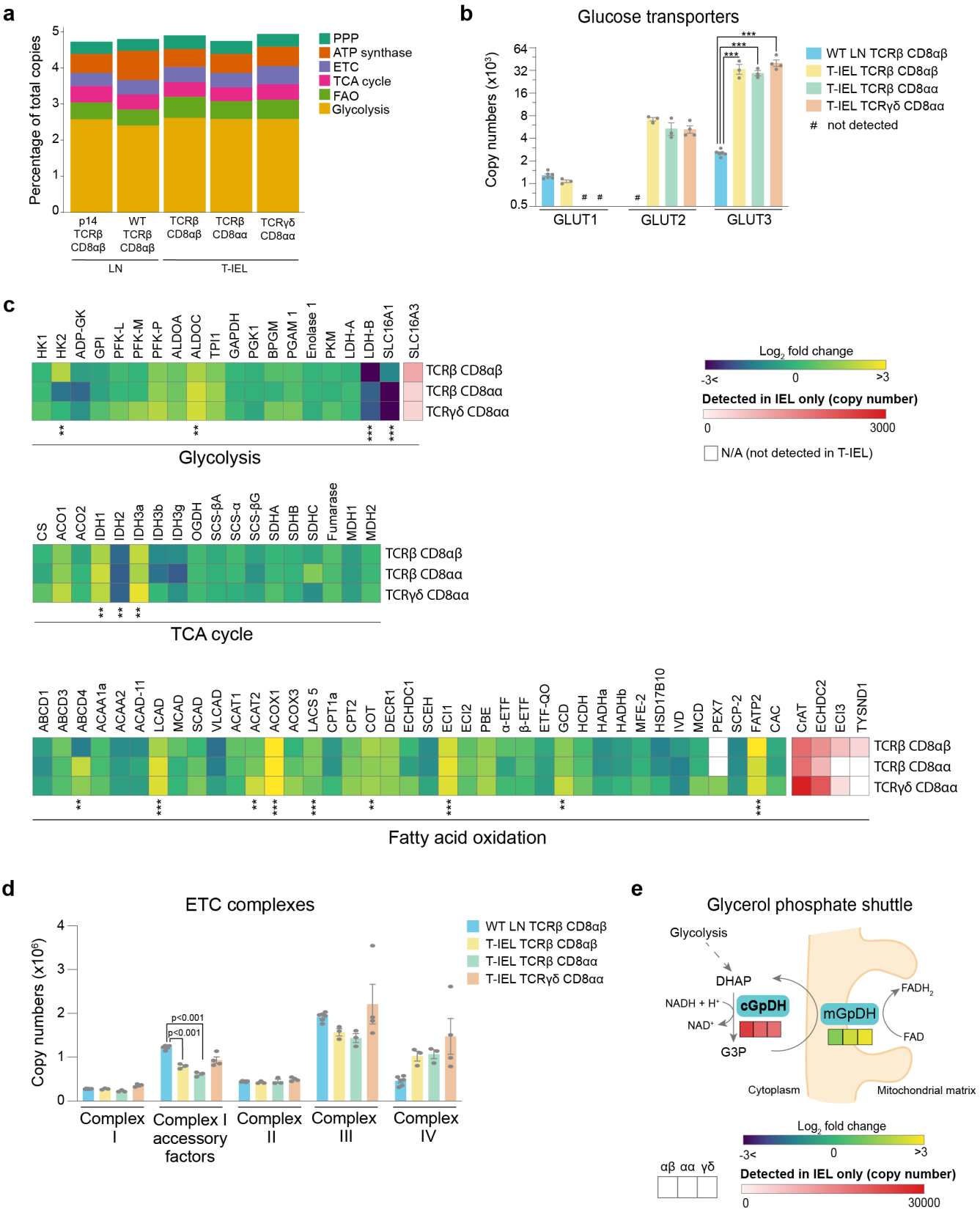
a
Percentage of total copies
PPP
ATP synthase
ETC
TCA cycle
FAO
Glycolysis
p14 TCRβ CD8αβ
WT TCRβ CD8αβ
TCRβ CD8αβ
TCRβ CD8αα
TCRγδ CD8αα
LN
T-IEL
b
Glucose transporters
Copy numbers (x10³)
WT LN TCRβ CD8αβ
T-IEL TCRβ CD8αβ
T-IEL TCRβ CD8αα
T-IEL TCRγδ CD8αα
not detected
GLUT1
GLUT2
GLUT3
c
HK1 HK2 ADP-GK GPI PFK-L PFK-M PFK-P ALDOA ALDOC TPI1 GAPDH PGK1 BPGM PGAM 1 Enolase 1 PKM LDH-A LDH-B SLC16A1 SLC16A3
TCRβ CD8αβ
TCRβ CD8αα
TCRγδ CD8αα
Glycolysis
Log2 fold change
-3< 0 >3
Detected in IEL only (copy number)
0 3000
N/A (not detected in T-IEL)
CS ACO1 ACO2 IDH1 IDH2 IDH3a IDH3b IDH3g OGDH SCS-βA SCS-α SCS-βG SDHA SDHB SDHC Fumarase MDH1 MDH2
TCA cycle
ABCD1 ABCD3 ABCD4 ACAA1a ACAA2 ACAD-11 LCAD MCAD SCAD VLCAD ACAT1 ACAT2 ACOX1 ACOX3 LACS 5 CPT1a CPT2 COT DECR1 ECHDC1 SCEH ECI1 ECI2 PBE α-ETF β-ETF ETF-QO GCD HCDH HADHa HADHb MFE-2 HSD17B10 IVD MCD PEX7 SCP-2 FATP2 CAC CrAT ECHDC2 ECI3 TYSND1
Fatty acid oxidation
d
ETC complexes
Copy numbers (x10⁶)
p<0.001
p<0.001
Complex I
Complex I accessory factors
Complex II
Complex III
Complex IV
e
Glycerol phosphate shuttle
Glycolysis
DHAP
NADH + H⁺
NAD⁺
cGpDH
G3P
mGpDH
FADH2
FAD
Cytoplasm
Mitochondrial matrix
αβ αα γδ
Log2 fold change
-3< 0 >3
Detected in IEL only (copy number)
0 30000

Figure 5

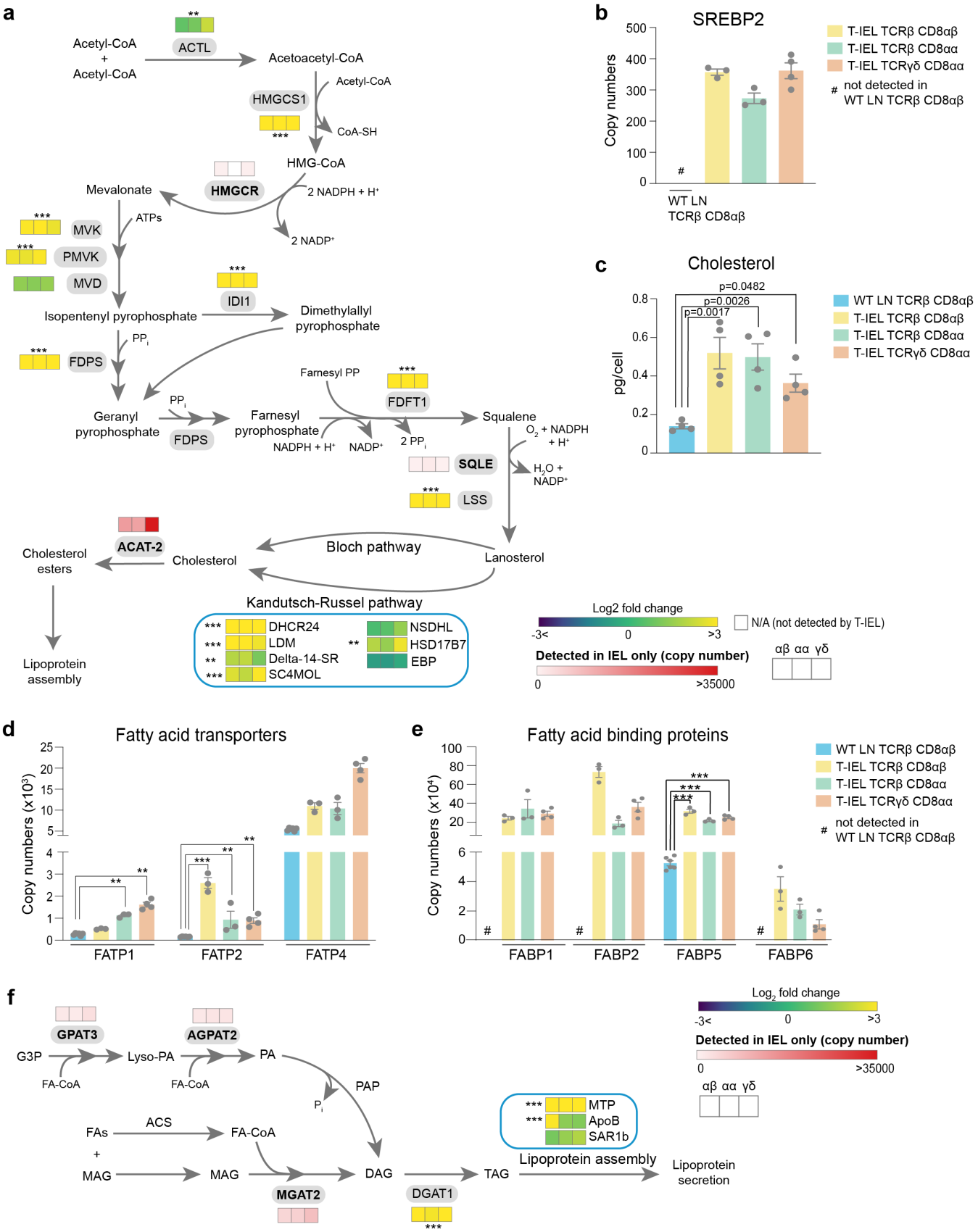
a
ACTL
Acetyl-CoA + Acetyl-CoA
Acetoacetyl-CoA
HMGCS1
Acetyl-CoA
CoA-SH
HMG-CoA
HMGCR
2 NADPH + H+
2 NADP+
Mevalonate
ATPs
MVK
PMVK
MVD
Isopentenyl pyrophosphate
IDI1
Dimethylallyl pyrophosphate
PPi
FDPS
Geranyl pyrophosphate
Farnesyl PP
FDFT1
Farnesyl pyrophosphate
NADPH + H+
NADP+
2 PPi
Squalene
O2 + NADPH + H+
H2O + NADP+
SQLE
LSS
Lanosterol
Bloch pathway
Cholesterol
ACAT-2
Cholesterol esters
Lipoprotein assembly
Kandutsch-Russel pathway
DHCR24
LDM
Delta-14-SR
SC4MOL
NSDHL
HSD17B7
EBP
Log2 fold change
-3<
0
>3
N/A (not detected by T-IEL)
Detected in IEL only (copy number)
0
>35000
αβ αα γδ
b
SREBP2
Copy numbers
WT LN TCRβ CD8αβ
T-IEL TCRβ CD8αβ
T-IEL TCRβ CD8αα
T-IEL TCRγδ CD8αα
not detected in WT LN TCRβ CD8αβ
c
Cholesterol
pg/cell
p=0.0482
p=0.0026
p=0.0017
WT LN TCRβ CD8αβ
T-IEL TCRβ CD8αβ
T-IEL TCRβ CD8αα
T-IEL TCRγδ CD8αα
d
Fatty acid transporters
Copy numbers (x10³)
FATP1
FATP2
FATP4
e
Fatty acid binding proteins
Copy numbers (x10⁴)
FABP1
FABP2
FABP5
FABP6
WT LN TCRβ CD8αβ
T-IEL TCRβ CD8αβ
T-IEL TCRβ CD8αα
T-IEL TCRγδ CD8αα
not detected in WT LN TCRβ CD8αβ
f
GPAT3
AGPAT2
G3P
Lyso-PA
PA
FA-CoA
FA-CoA
PAP
Pi
FAs + MAG
ACS
FA-CoA
MAG
MGAT2
DAG
DGAT1
TAG
MTP
ApoB
SAR1b
Lipoprotein assembly
Lipoprotein secretion
Log2 fold change
-3<
0
>3
Detected in IEL only (copy number)
0
>35000
αβ αα γδ

Figure 6

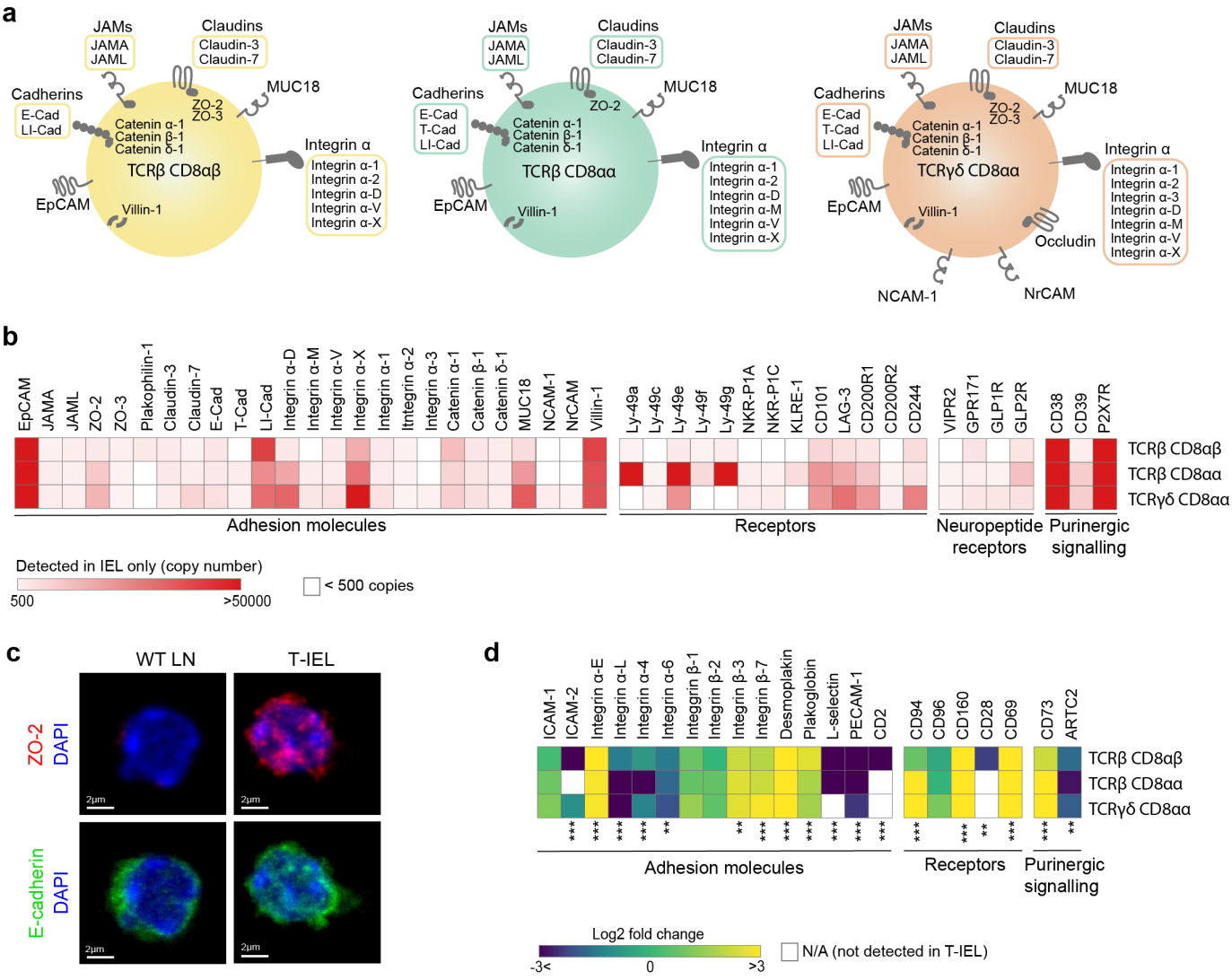
a
JAMs
JAMA
JAML
Claudins
Claudin-3
Claudin-7
Cadherins
E-Cad
LI-Cad
ZO-2
ZO-3
MUC18
Catenin α-1
Catenin β-1
Catenin δ-1
TCRβ CD8αβ
Integrin α
Integrin α-1
Integrin α-2
Integrin α-D
Integrin α-V
Integrin α-X
EpCAM
Villin-1
TCRβ CD8αα
Integrin α-M
TCRγδ CD8αα
T-Cad
Integrin α-3
Occludin
NCAM-1
NrCAM
b
EpCAM
JAMA
JAML
ZO-2
ZO-3
Plakophilin-1
Claudin-3
Claudin-7
E-Cad
T-Cad
LI-Cad
Integrin α-D
Integrin α-M
Integrin α-V
Integrin α-X
Integrin α-1
Itntegrin α-2
Integrin α-3
Catenin α-1
Catenin β-1
Catenin δ-1
MUC18
NCAM-1
NrCAM
Villin-1
Ly-49a
Ly-49c
Ly-49e
Ly-49f
Ly-49g
NKR-P1A
NKR-P1C
KLRE-1
CD101
LAG-3
CD200R1
CD200R2
CD244
VIPR2
GPR171
GLP1R
GLP2R
CD38
CD39
P2X7R
TCRβ CD8αβ
TCRβ CD8αα
TCRγδ CD8αα
Adhesion molecules
Receptors
Neuropeptide receptors
Purinergic signalling
Detected in IEL only (copy number)
500
>50000
< 500 copies
c
WT LN
T-IEL
ZO-2
DAPI
E-cadherin
DAPI
2μm
d
ICAM-1
ICAM-2
Integrin α-E
Integrin α-L
Integrin α-4
Integrin α-6
Integgrin β-1
Integrin β-2
Integrin β-3
Integrin β-7
Desmoplakin
Plakoglobin
L-selectin
PECAM-1
CD2
CD94
CD96
CD160
CD28
CD69
CD73
ART2
TCRβ CD8αβ
TCRβ CD8αα
TCRγδ CD8αα
Adhesion molecules
Receptors
Purinergic signalling
Log2 fold change
-3<
0
>3
N/A (not detected in T-IEL)

Figure 6- supplement figure 1

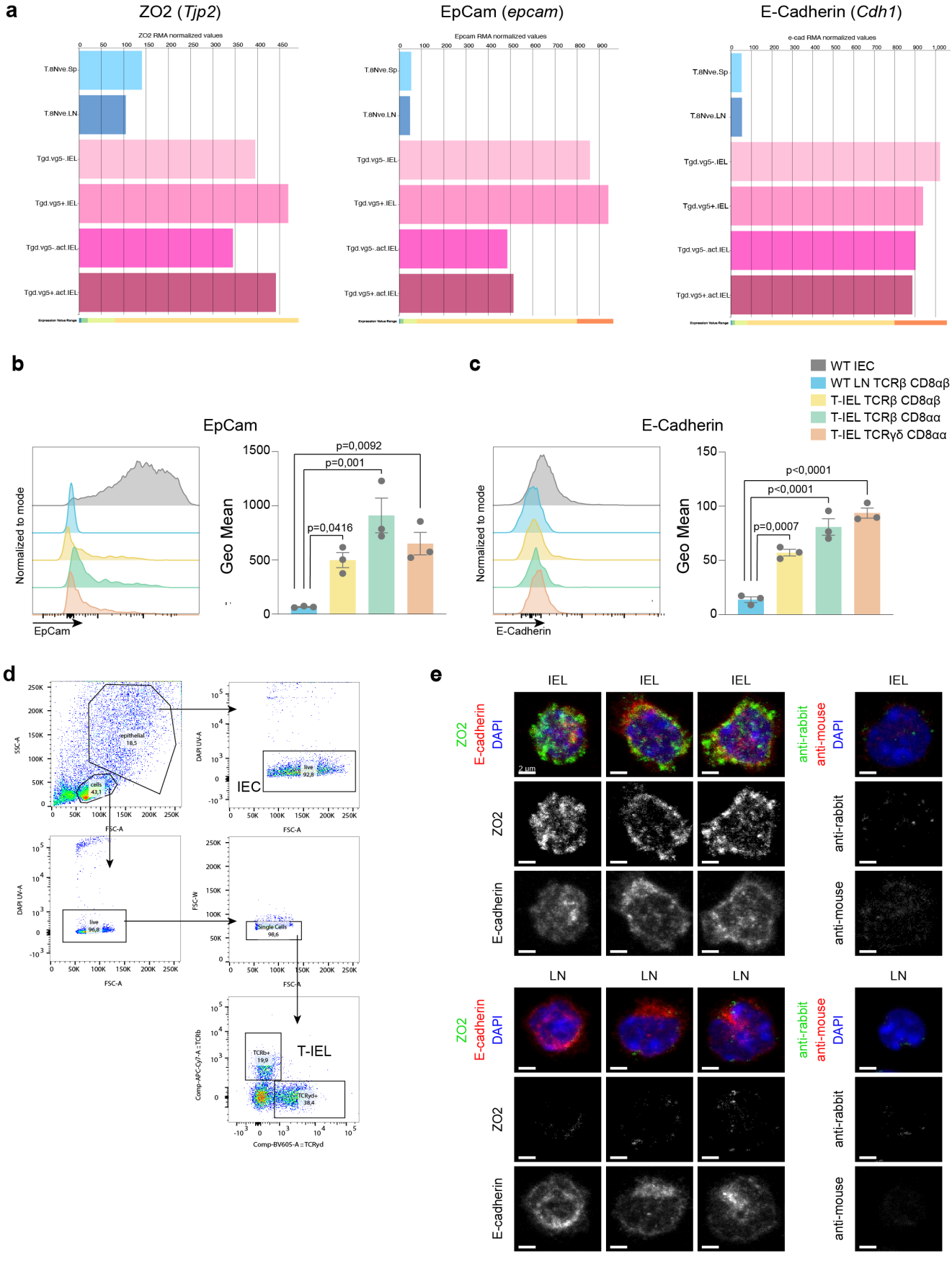

Figure 7

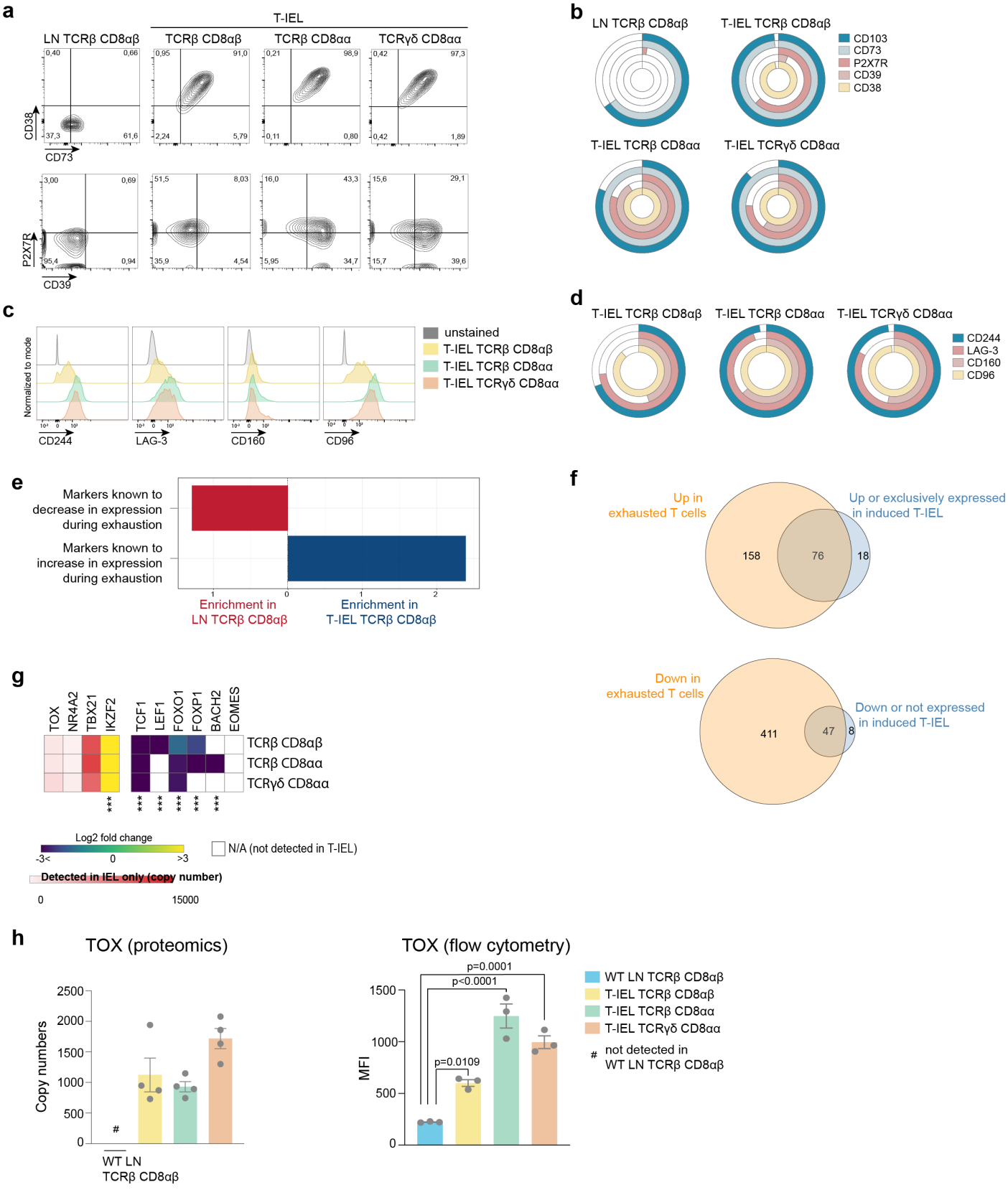
a
T-IEL
LN TCRβ CD8αβ
TCRβ CD8αβ
TCRβ CD8αα
TCRγδ CD8αα
CD38
CD73
P2X7R
CD39
b
LN TCRβ CD8αβ
T-IEL TCRβ CD8αβ
T-IEL TCRβ CD8αα
T-IEL TCRγδ CD8αα
CD103
CD73
P2X7R
CD39
CD38
c
Normalized to mode
unstained
T-IEL TCRβ CD8αβ
T-IEL TCRβ CD8αα
T-IEL TCRγδ CD8αα
CD244
LAG-3
CD160
CD96
d
T-IEL TCRβ CD8αβ
T-IEL TCRβ CD8αα
T-IEL TCRγδ CD8αα
CD244
LAG-3
CD160
CD96
e
Markers known to decrease in expression during exhaustion
Markers known to increase in expression during exhaustion
Enrichment in LN TCRβ CD8αβ
Enrichment in T-IEL TCRβ CD8αβ
f
Up in exhausted T cells
Up or exclusively expressed in induced T-IEL
158
76
18
Down in exhausted T cells
Down or not expressed in induced T-IEL
411
47
8
g
TOX
NR4A2
TBX21
IKZF2
TCF1
LEF1
FOXO1
FOXP1
BACH2
EOMES
TCRβ CD8αβ
TCRβ CD8αα
TCRγδ CD8αα
Log2 fold change
-3<
0
>3
N/A (not detected in T-IEL)
Detected in IEL only (copy number)
0
15000
h
TOX (proteomics)
Copy numbers
WT LN TCRβ CD8αβ
TOX (flow cytometry)
MFI
p=0.0001
p<0.0001
p=0.0109
WT LN TCRβ CD8αβ
T-IEL TCRβ CD8αβ
T-IEL TCRβ CD8αα
T-IEL TCRγδ CD8αα
not detected in WT LN TCRβ CD8αβ

Figure 8

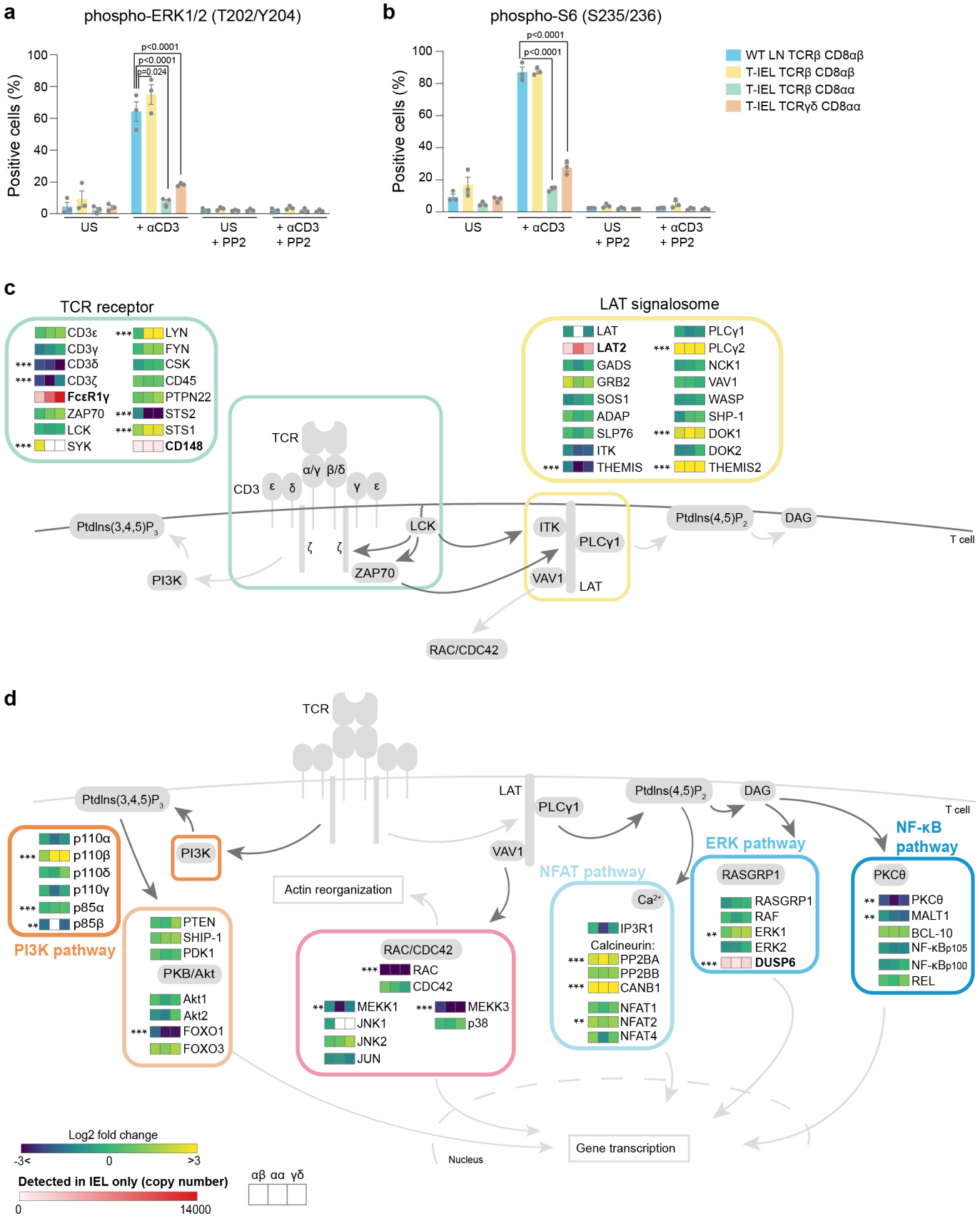
a
phospho-ERK1/2 (T202/Y204)
Positive cells (%)
p<0.0001
p<0.0001
p=0.024
US
+ αCD3
US + PP2
+ αCD3 + PP2
b
phospho-S6 (S235/236)
p<0.0001
p<0.0001
WT LN TCRβ CD8αβ
T-IEL TCRβ CD8αβ
T-IEL TCRβ CD8αα
T-IEL TCRγδ CD8αα
c
TCR receptor
CD3ε
CD3γ
CD3δ
CD3ζ
FcεR1γ
ZAP70
LCK
SYK
LYN
FYN
CSK
CD45
PTPN22
STS2
STS1
CD148
LAT signalosome
LAT
LAT2
GADS
GRB2
SOS1
ADAP
SLP76
ITK
THEMIS
PLCγ1
PLCγ2
NCK1
VAV1
WASP
SHP-1
DOK1
DOK2
THEMIS2
TCR
CD3
α/γ β/δ
ε δ γ ε
ζ ζ
LCK
ZAP70
PtdIns(3,4,5)P3
PI3K
ITK
PLCγ1
VAV1
LAT
PtdIns(4,5)P2
DAG
T cell
RAC/CDC42
d
TCR
PtdIns(3,4,5)P3
LAT
PLCγ1
PtdIns(4,5)P2
DAG
T cell
p110α
p110β
p110δ
p110γ
p85α
p85β
PI3K
PI3K pathway
VAV1
Actin reorganization
NFAT pathway
ERK pathway
NF-κB pathway
PTEN
SHIP-1
PDK1
PKB/Akt
Akt1
Akt2
FOXO1
FOXO3
RAC/CDC42
RAC
CDC42
MEKK1
MEKK3
JNK1
p38
JNK2
JUN
Ca2+
IP3R1
Calcineurin:
PP2BA
PP2BB
CANB1
NFAT1
NFAT2
NFAT4
RASGRP1
RASGRP1
RAF
ERK1
ERK2
DUSP6
PKCθ
PKCθ
MALT1
BCL-10
NF-κBp105
NF-κBp100
REL
Log2 fold change
-3<
0
>3
Detected in IEL only (copy number)
0
14000
αβ αα γδ
Nucleus
Gene transcription